

A comprehensive laboratory study on the immersion freezing behavior of illite NX particles: a comparison of seventeen ice nucleation measurement techniques

Naruki Hiranuma¹, Stefanie Augustin-Bauditz², Heinz Bingemer³, Carsten Budke⁴, Joachim Curtius³, Anja Danielczok³, Karoline Diehl⁵, Katharina Dreischmeier⁴, Martin Ebert⁶, Fabian Frank³, Nadine Hoffmann¹, Konrad Kandler⁶, Alexei Kiselev¹, Thomas Koop⁴, Thomas Leisner¹, Ottmar Möhler¹, Björn Nillius^{3,*}, Andreas Peckhaus¹, Diana Rose³, Stephan Weinbruch⁶, Heike Wex², Yvonne Boose⁷, Paul J. DeMott⁸, John D. Hader⁹, Thomas C. J. Hill⁸, Zamin A. Kanji⁷, Gourihar Kulkarni¹⁰, Ezra J. T. Levin⁸, Christina S. McCluskey⁸, Masataka Murakami¹¹, Benjamin J. Murray¹², Dennis Niedermeier^{2,**}, Markus D. Petters⁹, Daniel O'Sullivan⁹, Atsushi Saito¹¹, Gregory P. Schill¹³, Takuya Tajiri¹¹, Margret A. Tolbert¹³, André Welti⁷, Thomas F. Whale¹², Timothy P. Wright⁹, and Katsuya Yamashita^{11,***}

¹Institute for Meteorology and Climate Research – Atmospheric Aerosol Research, Karlsruhe Institute of Technology, Karlsruhe, Germany.

²Leibniz Institute for Tropospheric Research, Leipzig, Germany.

³Institute for Atmospheric Physics, University of Mainz, Mainz, Germany.

⁴Faculty of Chemistry, Bielefeld University, Bielefeld, Germany.

⁵Institute for Atmospheric and Environmental Science, Goethe University of Frankfurt, Frankfurt, Germany.

⁶Institute of Applied Geosciences, Technical University Darmstadt, Germany.

⁷Institute for Atmosphere and Climate Science, ETH, Zurich, Switzerland.

⁸Department of Atmospheric Science, Colorado State University, Fort Collins, CO, USA.

⁹Department of Marine Earth and Atmospheric Sciences, North Carolina State University, Raleigh, NC, USA.

¹⁰Atmospheric Science and Global Change Division, Pacific Northwest National Laboratory, Richland, WA, USA.

¹¹Meteorological Research Institute (MRI), Tsukuba, Japan.

¹²Institute for Climate and Atmospheric Science, School of Earth and Environment, University of Leeds, Leeds, UK.

¹³Cooperative Institute for Research in Environmental Sciences and Department of Chemistry and Biochemistry, University of Colorado, Boulder, CO, USA.

Now at, *Max-Planck-Institut für Chemie, Mainz, Germany.

Now at, **Department of Physics, Michigan Technological University, Houghton, MI, USA.

Now at, *** Snow and Ice Research Center, Nagaoka, Japan.

Manuscript in preparation for *Atmospheric Chemistry and Physics*
ACP – Special Issue: Results from the ice nuclei research unit (INUIT)

December 24, 2014

1 **Abstract**

2

3 Immersion freezing is the most relevant heterogeneous ice nucleation mechanism
4 through which ice crystals are formed in mixed-phase clouds. In recent years, an increasing
5 number of laboratory experiments utilizing a variety of instruments have examined immersion
6 freezing activity of atmospherically relevant ice-nucleating particles. However, an inter-
7 comparison of these laboratory results is a difficult task because investigators have used
8 different ice nucleation (IN) measurement methods to produce these results. A remaining
9 challenge is to explore the sensitivity and accuracy of these techniques and to understand how
10 the IN results are potentially influenced or biased by experimental parameters associated with
11 these techniques.

12 Within the framework of INUIT (Ice Nuclei research UnIT), we distributed an illite
13 rich sample (illite NX) as a representative surrogate for atmospheric mineral dust particles to
14 investigators to perform immersion freezing experiments using different IN measurement
15 methods and to obtain IN data as a function of particle concentration, temperature (T), cooling
16 rate and nucleation time. Seventeen measurement methods were involved in the data inter-
17 comparison. Experiments with seven instruments started with the test sample pre-suspended
18 in water before cooling, while ten other instruments employed water vapor condensation onto
19 dry-dispersed particles followed by immersion freezing. The resulting comprehensive
20 immersion freezing dataset was evaluated using the ice nucleation active surface-site density,
21 n_s , to develop a representative $n_s(T)$ spectrum that spans a wide temperature range ($-37\text{ }^\circ\text{C} < T$
22 $< -11\text{ }^\circ\text{C}$) and covers nine orders of magnitude in n_s .

23 In general, the seventeen immersion freezing measurement techniques deviate, within
24 a range of about $8\text{ }^\circ\text{C}$ in terms of temperature, by three orders of magnitude with respect to n_s .
25 In addition, we show evidence that the immersion freezing efficiency expressed in n_s of illite
26 NX particles is relatively independent of droplet size, particle mass in suspension, particle size
27 and cooling rate during freezing. A strong temperature dependence and weak time- and size
28 dependence of the immersion freezing efficiency of illite rich clay mineral particles enabled
29 the n_s parameterization solely as a function of temperature. We also characterized the $n_s(T)$
30 spectra and identified a section with a steep slope between -20 and $-27\text{ }^\circ\text{C}$, where a large
31 fraction of active sites of our test dust may trigger immersion freezing. This slope was
32 followed by a region with a gentler slope at temperatures below $-27\text{ }^\circ\text{C}$. While the agreement
33 between different instruments was reasonable below $\sim -27\text{ }^\circ\text{C}$, there seemed to be a different

34 trend in the temperature-dependent ice nucleation activity from the suspension and dry-
35 dispersed particle measurements for this mineral dust, in particular at higher temperatures. For
36 instance, the ice nucleation activity expressed in n_s was smaller for the average of the wet
37 suspended samples and higher for the average of the dry-dispersed aerosol samples between
38 about -27 and -18 °C. Only instruments making measurements with wet suspended samples
39 were able to measure ice nucleation above -18 °C. A possible explanation for the deviation
40 between -27 and -18 °C is discussed. Multiple exponential distribution fits in both linear and
41 log space for both specific surface area and geometric surface area are provided. These new
42 fits, constrained by using identical reference samples, will help to compare IN measurement
43 methods that are not included in the present study and IN data from future IN instruments.

44 1. Introduction

45

46 1.1. Background

47

48 Primary ice formation by atmospheric ice-nucleating particles (INPs) markedly
49 influences the formation and life cycle of mixed-phase clouds and very often also initiates
50 precipitation formation. Therefore, ice-containing clouds play a significant role in the energy
51 balance of the climate system and the hydrological cycle on Earth (Chapter 7 of IPCC 2013;
52 *Boucher et al.*, 2013). Currently, quantitative predictions for the impact of these clouds on the
53 Earth's radiative budget and thereby the climate are highly uncertain. This uncertainty arises
54 primarily from a lack of fundamental understanding of ice microphysical processes, the
55 representation of these processes in cloud models and knowledge of the abundance of INPs
56 (*Hoose and Möhler*, 2012; *Murray et al.*, 2012). In particular, yearly emission rates of soil
57 dust are 1000 to 4000 teragrams, accounting for a major proportion of both the dust
58 component and the total particle loading in the atmosphere (*Boucher et al.*, 2013). The
59 resulting radiative forcing directly exerted by mineral dust is estimated to range from -0.3 to
60 +0.1 W m⁻². Therefore, dust slightly contributes to the direct cooling effect of aerosols.
61 However, our understanding of the influence of the dust burden upon overall climate forcing,
62 including its secondary effect on cloud albedo, remains highly uncertain, in part due to the
63 absence of accurate INP representations in atmospheric models. Thus, the effective radiative
64 forcing effect of airborne dust on current climate predictions remains unresolved.

65 A small subset of all particles acts as INPs across a range of subzero temperatures,
66 triggering ice formation in clouds via the process of heterogeneous ice nucleation. Previous
67 laboratory experiments have taken diverse approaches in an attempt to mimic ice nucleation
68 and freezing processes. These heterogeneous ice formation processes include deposition
69 nucleation, immersion-, condensation- and contact freezing (*Vali*, 1985), inside-out contact
70 freezing (i.e., freezing of an immersed INP in contact with the droplet surface from the inside;
71 *Durant and Shaw*, 2005; *Fornea et al.*, 2009) and surface condensation freezing (i.e., freezing
72 of supercooled water or residual aqueous solution trapped on particle surfaces, e.g., by the
73 inverse Kelvin effect; *Christenson*, 2013; *Hiranuma et al.*, 2014a; *Marcolli*, 2014; *Welti et al.*,
74 2014; *Wex et al.*, 2014). Without INPs, pure cloud water droplets or solution within particles
75 can be supercooled to below -37 °C before freezing (*Koop et al.*, 2000; *Murray et al.*, 2010;
76 *Rosenfeld and Woodley*, 2000).

77 Among the various modes of atmospheric ice nucleation, immersion freezing is one of
78 the most important mechanisms for primary ice formation, accounting for 85% of ice
79 formation in clouds that contain supercooled droplets (*Hoose et al.*, 2010). Furthermore, many
80 of the previous experimental studies have investigated heterogeneous ice nucleation at
81 conditions where water is supercooled before freezing (e.g., *Murray et al.*, 2012). However,
82 the relative importance of the particles' physico-chemical properties [i.e., size, composition,
83 solubility, hygroscopicity, cloud condensation nuclei activity, ice nucleation (IN) active sites,
84 surface charge and/or crystallographic structure] for immersion freezing is not yet well known
85 (e.g., *Hiranuma et al.*, 2013; *Hiranuma et al.*, 2014b; *Murray et al.*, 2012). Hence, more in-
86 depth investigations and understanding of heterogeneous ice nucleation processes in
87 supercooled clouds (as well as mixed-phase clouds) is of particular importance.

88

89 **1.2. State of the art of IN measurement techniques**

90

91 The concept of condensation nuclei contributing to ice formation was first introduced
92 by Alfred Wegener in 1911 (*Wegener*, 1911). Since then, various instruments and methods
93 have been developed to investigate the composition of atmospherically relevant INPs as well
94 as their abundance; for example, the rapid expansion cloud-simulation chamber (RECC) was
95 first introduced as a detector of ionizing particles. Such instruments have been used in many
96 ice nucleation studies since the 1940s (e.g., *Cwilong*, 1947; *Fournier d'Albe*, 1949; *Palmer*,
97 1949; *Bigg*, 1957; *Kline and Brier*, 1961). Supersaturated conditions with respect to water and
98 ice, as a function of temperature, are created in the RECC vessel by a rapid pressure drop
99 caused by mechanical expansion and concomitant cooling. Subsequently, water vapor in the
100 supersaturated air can either deposit or condense on sample particles, leading to the formation
101 of water droplets and/or ice.

102 A different type of instrument widely used to measure abundance and efficiency of
103 INPs is the continuous flow diffusion chamber (CFDC). The need for portable instruments
104 capable of obtaining continuous measurements for aircraft applications emerged in
105 discussions during the 1970s and was a main driver of CFDC development. In CFDCs,
106 particles are sampled into a region between two ice-coated concentric cylinders (or dual
107 parallel plates) maintained at different temperatures, which generates a region of ice
108 supersaturation between ice-coated walls. As the particles experience ice supersaturation
109 conditions for a few seconds, INPs can be activated and diffusively grow to supermicron ice
110 crystals. Typically, these large ice crystals can be detected and counted by an optical particle

111 counter (OPC) downstream of the instrument while the chamber temperature and humidity
112 conditions are continuously recorded. Since its first appearance in the 1980s with horizontal
113 parallel plates (*Hussain and Saunders, 1984; Tomlinson and Fukuta, 1985*), several new
114 designs and operational principles have been introduced (e.g., vertically oriented cylinders;
115 *Rogers et al., 1988*, horizontally oriented parallel plates; *Kanji and Abbatt, 2009*, vertically
116 oriented parallel plates; *Stetzer et al., 2008; Chou et al., 2011; Friedman et al., 2011*). An
117 alternative configuration is the continuous flow mixing chamber (e.g., Fast Ice Nucleus
118 Chamber or FINCH; *Bundke et al., 2008*). The operation principle of this type of chamber
119 does not involve water vapor diffusion from the ice walls, as in CFDC, but water vapor is
120 available for ice growth from the humidified air within the chamber flow. This leads to an
121 upper limit on INP concentrations that are observable with this methodology (*DeMott et al.,*
122 *2011*). A flow tube (e.g., Leipzig Aerosol Cloud Interaction Simulator or LACIS, *Hartmann*
123 *et al., 2011*) has also been developed in which a humidified stream containing aerosol
124 particles is first cooled to activate droplets on the particles, which upon further cooling may
125 then freeze.

126 In addition to chamber techniques, the mode-specific conditions for heterogeneous ice
127 nucleation of a known INP placed on a substrate surface have been studied using optical
128 microscope techniques. For example, by immersing ice nuclei in water droplets placed on a
129 hydrophobic substrate surface and collecting a series of images at controlled cooling rates, the
130 change in reflectivity and opacity following ice formation can be characterized, and the
131 associated freezing conditions can be identified (e.g., *Knopf and Alpert, 2013; Murray et al.,*
132 *2011*). More recently, other optical microscopy techniques coupled with a unique method of
133 encapsulating particles into droplets followed by cooling (*Iannone et al., 2011*) or using the
134 hydrophobic squalene/water emulsion (*Wright and Petters, 2013*) were introduced to the
135 community. Using a similar approach, substrate-supported cooling studies have been applied
136 to determine the freezing temperature in the contact mode (e.g., *Fornea et al., 2009; Niehaus*
137 *et al., 2014*), or of deposition nucleation (e.g., *Kanji and Abbatt, 2006; Bingemer et al., 2012;*
138 *Dymarska et al., 2006*). The microscopy-coupled substrate-supported freezing devices are
139 advantageous to visualize the consequences of specific ice nucleation modes in controlled and
140 simulated environments. In some studies, immersion freezing of microliter scale droplet
141 volumes was analyzed at temperatures (T_s) higher than $-10\text{ }^\circ\text{C}$ with a sensitivity of INP
142 concentration as good as $\sim 10^{-5}\text{ L}^{-1}$ (*Ardon-Dreyer et al., 2011*).

143 The freezing temperature of INPs either immersed in or in contact with levitated
144 supercooled water droplets suspended in the air can also be determined by the change in light

145 scattering with a charge-coupled device (CCD) camera using an electrodynamic balance
146 (EDB; *Hoffmann et al.*, 2013), an acoustic levitator (*Diehl et al.*, 2014) or in a vertical wind
147 tunnel (*Szakáll et al.*, 2009). The advantage of these methods is the ability to provide, via
148 high-resolution images, substrate-free information for statistically representative ice
149 nucleation processes on a single droplet basis. This advantage is shared with all of the above
150 mentioned chamber and flow tube devices.

151 Undoubtedly, these enormous efforts to develop numerous IN measurement techniques
152 have advanced our basic knowledge of atmospheric ice formation. As a consequence, the
153 atmospheric science community will continue to pursue investigations of IN to unravel their
154 associated effects on climate. Accordingly, exploring the sensitivities, uncertainties and biases
155 of various experimental techniques (e.g., methods for particle generation, size segregation,
156 size estimation, ice detection and any other notable experimental procedures) in nucleating ice
157 on particles of known physico-chemical properties is crucial in order to compile comparative
158 INP data of multiple and complex measurement techniques from various research institutions.
159 The information obtained from one technique guides other measurement techniques (*DeMott*
160 *et al.*, 2011; *Riechers et al.*, 2013). A better understanding of the sensitivity of multiple
161 techniques and the role of associated experimental parameters upon INP measurements will
162 also help in transferring the laboratory-based measurements of INPs of various atmospheric
163 constituents to their reliable parameterizations in models of atmospheric processes.

164 Since the 1960s, four international workshops have been organized to compare the
165 performance of IN measuring instruments that were emerging or available at the time (*DeMott*
166 *et al.*, 2011). In particular, effort was made during the fourth international ice nucleation
167 workshop in 2007 (ICIS-2007) to assemble a total of nine laboratory and field IN instruments
168 at the AIDA (Aerosol Interaction and Dynamics in the Atmosphere) facility and compare
169 them using identical test dust samples (e.g., Arizona Test Dust, or ATD, and Saharan dust)
170 over similar thermodynamic conditions. State-of-the-art knowledge was obtained from each
171 workshop activity, and such measurement understanding was further incorporated to develop
172 the next generation of IN instruments.

173

174 **1.3. Objectives**

175

176 The major aim of this study, and concurrent studies within the framework of the
177 INUIT (Ice Nuclei research UnIT) project, is to investigate the immersion freezing behavior
178 of reference particles (e.g., Snomax for bacterial IN processes and potassium rich feldspar, K-

179 feldspar, for mineral dust IN processes). In this work, we distributed illite NX samples from
180 the same batch [with the exceptions of the samples used for Leeds-NIPI, ZINC and IMCA-
181 ZINC (acronyms are defined in the Supplementary Information Sect. S4); *Broadley et al.*,
182 2012; *Welti et al.*, 2009] among the INUIT project and associated partners. With a total of
183 seventeen different IN measuring instruments, we inter-compared IN data from each
184 instrument in order to obtain a comprehensive dataset for evaluating immersion freezing
185 properties of illite NX particles. The dataset captures the functional dependence of various
186 experimental parameter variables, such as particle concentration, particle size, droplet size,
187 temperature, cooling rate and nucleation time, on the immersion freezing properties of illite
188 NX particles. Further, some instruments used test samples suspended in water prior to
189 experiments, while others used dry-dispersed particles. The basic experimental methods and
190 parameterization approaches used to interpret the overall results and perform the inter-
191 comparison are discussed.

192 Results of freezing efficiencies at specific temperatures are presented using the ice
193 nucleation active surface-site density (n_s) parameterization (e.g., *Connolly et al.*, 2009;
194 *Niemand et al.*, 2012; *Hoose and Möhler*, 2012) developed on the basis of suggestions by
195 *DeMott et al.* (1995). For instance, *Niemand et al.* (2012) showed that the singular
196 parameterization approach of immersion freezing (i.e., freezing along water saturation
197 conditions while cooling) of various desert dust particles derived from AIDA experiments
198 converge upon one representative fit as a function of temperature, which is valid across a
199 temperature range from -12 to -36 °C. The time-independent n_s parameterization has also been
200 used in describing INP activation by several different constituents of clay minerals, e.g.,
201 microcline and kaolinite, using the cold stage droplet freezing technique (*Atkinson et al.*,
202 2013; *Murray et al.*, 2011; *Murray et al.*, 2010). Hence, comparison of IN efficiencies can be
203 readily performed for multiple types of instruments using n_s parameterizations. Moreover,
204 such time-independent and surface-area-scaled n_s formulations can be further adapted to
205 comprehensively assess ice nucleation in a wide range of atmospherically relevant
206 temperatures and relative humidities with respect to ice (RH_{ice}), as was recently presented in
207 *Hiranuma et al.* (2014a). The n_s parameterization for both immersion freezing and deposition
208 nucleation can be directly implemented in cloud, weather and climate models to calculate the
209 temperature-dependent abundance of INPs as a function of the aerosol surface area
210 concentration.

211 2. Methods

212

213 2.1. Illite NX characterization

214

215 In this study, we have chosen illite NX (Arginotec, NX Nanopowder) as a surrogate
216 for natural desert dusts. This choice of an illite rich material is based on a comparison of its
217 mineralogical composition to that of desert dusts, which are also rich in illite but are also
218 mixed with a range of other minerals (*Broadley et al.*, 2012). The present work gives an
219 overview of laboratory experiments for immersion freezing of particles of illite NX, used as a
220 surrogate for atmospheric desert dust particles. Illite NX bulk powder was previously
221 characterized for its physico-chemical properties, such as mineralogy and specific surface area
222 (SSA or θ for brevity). It was observed that illite NX samples contained more than 74 weight
223 percent (wt%) illite (*Broadley et al.*, 2012; *Friedrich et al.*, 2008) along with other
224 components [kaolinite, quartz, calcite and feldspars (most likely orthoclase/sanidine), see
225 Sect. 3.1 for more detail] which is similar to the X-ray diffraction (XRD) data specified by the
226 manufacturer. These test particles typically have aggregates of many nanometer-sized grains,
227 yielding an order of magnitude greater SSA ($104.2 \text{ m}^2 \text{ g}^{-1}$; *Broadley et al.*, 2012). The
228 aspherical and elongated nature of illite NX particles (aspect ratio up to ~ 4.8 ; *Veghte and*
229 *Freedman*, 2014) emphasizes the importance of considering its irregular shape. The
230 manufacturer reports the particle density, after mechanical granulation, as 2.65 g cm^{-3} .

231 To determine the purity of our sample, and to compare this with previous observations,
232 the dust mineralogy of a bulk illite NX sample was characterized using XRD (*Waseda et al.*,
233 2011) prior to distribution. In addition, complementary energy dispersive X-ray (EDX)
234 spectroscopy analysis was performed to characterize the elemental composition of individual
235 particles. The illite NX particles were sampled directly from the AIDA chamber using a 47
236 mm Nuclepore[®] filter (Whatman, 0.2 μm pore-size, filter Cat. No. 111106) and used in the
237 EDX analysis.

238 The N_2 -adsorption-based SSA (or BET surface, *Brunauer, Emmett, and Teller*, 1938)
239 of the illite NX sample was also measured. BET is a gas adsorption technique where the
240 quantity of various gases required to form a monolayer over the entire available surface of dry
241 particles, including internal surfaces, is measured (*Gregg and Sing*, 1982; *Bickmore et al.*,
242 2002). From the knowledge of the size of a molecule on the surface, it is possible to
243 determine the total surface area (S_{total}). In this work, BET surface areas were determined using

244 two different gas adsorbents: N₂ and H₂O (resulting in θ_{N_2} and θ_{H_2O}), with the latter being the
245 surface area exposed to water. BET measurements with H₂O were limited to 28% relative
246 humidity with respect to water (RH_w) to correctly account for a monolayer of H₂O
247 (*Quantachrome Instruments*, 2013).

248 The effect of particle processing, such as removal of hydrophilic ions by water, in a
249 water suspension was examined by ion chromatography (IC). The influence of dust washing
250 and discharge of soluble materials on IN propensity has been previously proposed (*Welti et*
251 *al.*, 2014). More specifically, the authors postulated two different scenarios at different
252 temperatures based on their observations. At temperatures below ~ -38 °C, the washed dust
253 component may have enhanced water condensation below water saturation, and a formed
254 liquid layer presumably may have stabilized the subcritical ice embryo entrapped inside the
255 liquid. The authors proposed this capillary condensation process as a part of condensation
256 freezing or homogeneous nucleation based on the previous observation (*Christenson*, 2013)
257 and the theoretical framework (*Marculli*, 2013). Above ~ -38 °C, on the other hand,
258 heterogeneous nucleation might have been suppressed because the liquid layer derived from
259 the deliquescence of soluble impurities from individual particles may have diminished
260 accessibility of water vapor to active sites (e.g., localized surface features such as cracks and
261 edges), originally proposed by *Koehler et al.* (2010), preventing the ice embryo formation. In
262 this study, suspended samples were prepared by stirring illite NX powders (0.1 g in 10 mL of
263 18.2 MΩ cm nanopure water) over three weeks. IC (Dionex DX-500 IC System equipped with
264 Dionex CD20 Conductivity Detector) was used to determine the concentrations of washed out
265 cations (K⁺, Ca²⁺ and Mg²⁺) as a function of time. A weak solution of sulfuric acid [5mL
266 H₂SO₄ (96 wt%) diluted in 2 L of Nanopure water] was used as the eluent. The measurements
267 were conducted in three series: every 5 to 10 s (seconds) within the first 2 min (minutes)
268 (ultra-short time series, USTS), then every 10 min within the first hour after immersion (short
269 time series, STS) followed by a long time series (LTS) with cation concentration
270 measurements conducted every 2 days thereafter for a three week period.

271

272 **2.2. Particle size distribution**

273

274 Size distributions and the S_{total} (in m² cm⁻³) of both suspended and dry-dispersed illite
275 NX particles were characterized using four size measurement techniques (i.e., aerosol size
276 spectrometers and light scattering instruments). In particular, the dynamic light scattering

277 (DLS) size of suspended illite NX particles (0.05 to 1 mg bulk illite NX sample in 1 mL of
278 triple-distilled water) was determined using the StabiSizer[®] (Microtrac Europe GmbH, PMX
279 200CS) over the range of 0.0008 to 6.5 μm hydrodynamic diameter. A more detailed
280 description of this instrument and its application for studying the size of particles in
281 suspension are addressed in *Hiranuma et al.* (2014b), and only a brief discussion is given
282 here. The DLS measurements were carried out with negligible contribution of multiple
283 scattering due to the utilized 180° backscattering mode. The hydrodynamic diameter, which
284 was comparable to the volume equivalent diameter, is determined using a refractive index of
285 1.55 to 1.58 for illite and of 1.333 for water, and a viscosity of water of 1.002 and 0.797 mPa
286 s at 20 and 30 °C, respectively. From this metric, the surface area was calculated assuming
287 spherical particles.

288 Size distributions of dry polydisperse illite NX particles were measured at AIDA
289 controlled expansion cloud-simulation chamber (CECC) and MRI dynamic CECC (DCECC)
290 prior to the expansion experiments. For AIDA-CECC, de-agglomerated illite NX particles
291 from a rotating brush disperser (PALAS, RGB 1000) were passed through a series of inertial
292 cyclone impactor stages ($D_{50} \sim 1$ and 5 μm) and introduced to the 84 m³ volume AIDA vessel.
293 Subsequently, a scanning mobility particle sizer (SMPS, TSI Inc., Model 3081 differential
294 mobility analyzer, DMA, and Model 3010 condensation particle counter, CPC) and an
295 aerodynamic particle sizer (APS, TSI Inc., Model 3321) were used to measure particle size
296 distributions over the range of 0.01 to 15.4 μm volume equivalent diameter. The assumption
297 of particle sphericity, a dynamic shape factor (DSF or χ in equations) of 1.49 ± 0.12 (average
298 of ten measurements \pm standard deviation) and a particle density of 2.65 g cm⁻³ were used to
299 obtain the geometric-based (volume equivalent) diameter from an APS (*Hiranuma et al.*,
300 2014b). At MRI-DCECC, a combination of an SMPS (TSI Inc., Model 3936) and a welas
301 optical particle counter (welas-OPC, PALAS, Sensor series 2500) was used to acquire a size
302 distribution for the size range of 0.01 to 47.2 μm volume equivalent diameter directly from the
303 1.4 m³ volume vessel. The same disperser type was used at both chambers for particle
304 generation, and the upstream cyclone impactors ($D_{50} \sim 1$ and 2.5 μm) were similarly deployed
305 to filter out any larger particles and safeguard against injecting these particles into the vessel.
306 We note that a linear correction factor of ~ 2 was applied to convert the optical diameter
307 measured by the welas-OPC to the APS-inferred volume equivalent diameter in several
308 studies (*Wagner et al.*, 2011; *Hiranuma et al.*, 2014a).

309 The particle number size distribution of dry particles in the 0.3-10 μm diameter range
310 was also measured by a TSI 3330 optical particle sizer (OPS, TSI Inc.; TSI-OPS hereafter).

311 For particle generation, the illite NX sample was dispersed using a magnetic stirrer in a 100
312 mL glass vessel that was purged with 200 mL min⁻¹ of dry particle-free compressed laboratory
313 air, and then diluted further in two stages by approximately 1:100 with dry air. Subsequently,
314 the backward scattering intensity of scattered light from a particle illuminated by a laser ($\lambda =$
315 660 nm) was measured. The instrument estimated the particle size distribution, assuming
316 spherical particles, using Mie theory. As a result, the reported size is a volume equivalent
317 spherical diameter. Additionally, these dry-dispersed particles were used for the immersion
318 mode experiments of FRIDGE as described in the Supplementary Methods.

319

320 **2.3. Ice nucleation measurements**

321

322 The ice nucleation measurement techniques contributing to this collaborative effort are
323 listed in Table 1. Descriptions of each measurement technique and their acronyms are
324 available in the Supplementary Information Sect. S4. Briefly, four CFDC-type instruments,
325 one continuous flow mixing chamber, two cloud simulation chambers, one diffusion cell, two
326 levitators, one vertical wind tunnel, one laminar flow tube and five cold stage-type systems
327 were employed in the inter-comparison. As seen in Table 1, measurement techniques with the
328 first seven instruments (i.e., ID 1 to 7) and the immersion mode measurements of FRIDGE
329 (ID 12) examined droplets produced from bulk illite NX samples in suspension, while the rest
330 used dry-dispersed illite NX powder, sometimes followed by size selection with a DMA.
331 Methods working with suspensions and those using dry particles employed different ways to
332 determine the particle surface area, and the influence of these differences on the determination
333 of n_s was investigated. For instance, CSU-IS was used to investigate the freezing activity of
334 both bulk suspension and size-segregated particles in suspension. Two cloud expansion
335 chambers, AIDA-CECC and MRI-DCECC, examined both polydisperse and size-selected dry
336 illite NX particles. LACIS and IMCA-ZINC measured immersion freezing of droplets, where
337 each droplet contained a single particle, and examined differently sized dry particles. The role
338 of IN modes upon the estimation of n_s was also examined across various temperature ranges.
339 The EDB-based method was used to measure the contact and immersion mode efficiencies of
340 size segregated dry illite NX particles around -30 °C. Immersion freezing results from IMCA-
341 ZINC were compared to previously reported ZINC data (*Welti et al.*, 2009) at temperatures
342 below -31 °C and to PINC data for temperatures below -26 °C. In the present study, we
343 derived ZINC's n_s values from the results reported in *Welti et al.* (2009). Specifically, ice

344 formation above 105% RH_w up to the water drop survival line was used to calculate n_s based
345 on given illite NX particle sizes. We note that the latent heat of condensation has minimal
346 impact on droplet temperature, such that RH_w > 105% maintains a water supersaturating
347 condition for droplet freezing.

348 FRIDGE investigated ice nucleation of both dry-dispersed particles on a substrate at
349 fixed temperatures ($-25\text{ }^\circ\text{C} < T < -18\text{ }^\circ\text{C}$) with increasing humidity ('default' deposition mode
350 nucleation) as well as immersed particles. In the case of immersion freezing experiments with
351 suspended samples, the cell temperature was lowered by $1\text{ }^\circ\text{C min}^{-1}$.

352 The range of mass concentrations of the bulk illite NX sample in suspension varied
353 from 3.1×10^{-6} wt% (CSU-IS) to 2.6 wt% (M-WT). For dry-dispersed particle measurements,
354 particle concentrations varied from $\sim 10\text{ cm}^{-3}$ (AIDA) up to $\sim 9000\text{ cm}^{-3}$ (MRI-DCECC).
355 Experiments with M-AL, M-WT, EDB, and IMCA-ZINC were performed on a single drop
356 basis. The shortest residence time of roughly 1.6 s was used for the laminar flow tube, LACIS,
357 and the slowest cooling rate of $0.3\text{ }^\circ\text{C min}^{-1}$ (time-average cooling rate over an expansion,
358 which translates to the equivalent updraft rate of $\sim 0.5\text{ m s}^{-1}$) was used in AIDA-CECC.
359 Altogether, immersion freezing was examined across the temperature range from ~ -10 to $\sim -$
360 $38\text{ }^\circ\text{C}$, and over a varied range of cooling rates, nucleation times and particle concentrations
361 (summarized in publically accessible data base available at [http://imk-aaf-s1.imk-](http://imk-aaf-s1.imk-aaf.kit.edu/inuit/)
362 [aaf.kit.edu/inuit/](http://imk-aaf.kit.edu/inuit/)).

363

364 **2.4. Ice nucleation parameterization**

365

366 We now describe a method to parameterize surface area-scaled immersion freezing
367 activities using the size equivalent ice nucleation active surface-site density based on
368 geometric size ($n_{s,\text{geo}}$; *Connolly et al., 2009; Niemand et al., 2012; Hoose and Möhler, 2012*).
369 In short, this surface-site density approach approximates ice crystal formation observed in an
370 experiment as a function of temperature, thus not accounting for time dependence.

371 Accordingly, $n_{s,\text{geo}}$ can be expressed by:

$$372 \quad n_{s,\text{geo}}(T) = -\ln\left(1 - \frac{N_{\text{ice}}(T)}{N_{\text{total}}}\right) \left(\frac{1}{S_{\text{ve}}}\right), \quad (1)$$

373 in which, N_{ice} is the number concentration of formed ice crystals (cm^{-3}), N_{total} is the total
374 number concentration of particles prior to any freezing event (cm^{-3}), and S_{ve} is the volume

375 equivalent surface area of an individual particle (m^2). As demonstrated in *Niemand et al.*
 376 (2012), if the activated ice fraction is small (<0.1), the Taylor series approximation can be
 377 applied to Eqn. 1. Assuming a uniform distribution of $n_{s,\text{geo}}$ over a given S_{total} and a size
 378 independency of $n_{s,\text{geo}}$, we can approximate $n_{s,\text{geo}}$ as:

$$379 \quad n_{s,\text{geo}}(T) \approx \frac{N_{\text{ice}}(T)}{N_{\text{total}}S_{\text{ve}}} = \frac{N_{\text{ice}}(T)}{S_{\text{total}}}. \quad (2)$$

380 In addition, the IN efficiency can be related to the BET-SSA to estimate BET-inferred
 381 ice nucleation surface-site density, $n_{s,\text{BET}}$. A description of the procedures used to estimate
 382 both n_s metrics is given in *Hiranuma et al.* (2014b). The advantage of using $n_{s,\text{geo}}$ is its
 383 applicability to both measurements and modeling activities due to the assumption of particle
 384 sphericity. Conversely, $n_{s,\text{geo}}$ cannot be directly obtained through suspension experiments
 385 because the size distribution of a suspended sample for each experiment is not available;
 386 therefore, S_{total} is determined from BET and the sample mass suspended in water.

387 In order to convert $n_{s,\text{geo}}$ values of all dry-dispersed particle measurements into $n_{s,\text{BET}}$,
 388 the geometric size-based ice-nucleating mass, $n_{m,\text{geo}}$ (g^{-1}), is first calculated from the IN active
 389 surface using either the surface-to-mass conversion factor (in $\text{m}^2 \text{g}^{-1}$) of $6/D_{\text{ve}}\rho$ (size-selected
 390 case) or $S_{\text{total}}/M_{\text{total}}$ (polydisperse case) by:

$$391 \quad n_{m,\text{geo}}(T) = \frac{N_{\text{ice}}(T)}{N_{\text{total}}M_{\text{ve}}} = \frac{6}{D_{\text{ve}}\rho} n_{s,\text{geo}}(T) \approx \left(\frac{S_{\text{total}}}{M_{\text{total}}} \right) n_{s,\text{geo}}(T) \quad (3)$$

392 where M_{ve} is the mass of a spherical particle of volume-equivalent diameter (g), D_{ve} is the
 393 volume equivalent midpoint diameter of particles (m), ρ is the particle density of illite NX
 394 ($2.65 \times 10^6 \text{ g m}^{-3}$), and M_{total} is the total particle mass concentration (g cm^{-3}). We note that the
 395 DLS size distribution-derived $S_{\text{total}}/M_{\text{total}}$ (i.e., DLS-SSA) is $6.54 \text{ m}^2 \text{g}^{-1}$ and use for the
 396 measurements with suspended particles. We also note that the conversion factor ranges from
 397 11.3 to $2.26 \text{ m}^2 \text{g}^{-1}$ for size-selected particle diameters from 200 nm to 1000 nm , respectively,
 398 where these sizes denote the range of particle diameters used in the size-selected cases in the
 399 present study. Therefore, ice-nucleating mass can be scaled to the BET-SSA (θ , $124.4 \text{ m}^2 \text{g}^{-1}$)
 400 to derive $n_{s,\text{BET}}$ as:

$$401 \quad n_{s,\text{BET}}(T) = \frac{n_{m,\text{geo}}(T)}{\theta} \approx \frac{n_{m,\text{sus}}(T)}{\theta} = \frac{\alpha}{M_{\text{ve}}\theta}, \quad (4)$$

402 in which, $n_{m,\text{sus}}$ is the IN active mass for suspension measurements, α represents the ice
 403 activated fraction ($= N_{\text{ice}}/N_{\text{total}}$), which is the direct measurement of suspension experiments
 404 and some of the dry-dispersed particle methods. With an assumption of a uniform BET-SSA,

405 the resulting $n_{s,BET}$ may be representative of measurements with suspended samples because
406 minimal corrections (only α and θ) are involved when compared to that with dry-dispersed
407 particles. Owing to internal surface area and surface roughness, BET-SSA may be greater than
408 DLS-SSA (*O'Sullivan et al.*, 2014).

409 Alternatively, we can also convert ice-nucleating mass derived from suspension
410 measurements, $n_{m,sus}$, to $n_{s,geo}$ using DLS-SSA to provide a reasonable comparison to dry-
411 dispersed particle measurements. However, this process requires one more step than when
412 using $n_{s,BET}$ (with an additional assumption of constant size distribution for all suspensions)
413 and two more steps than when using n_m . For our inter-comparison study, we used both $n_{s,BET}$
414 and $n_{s,geo}$. Because fewer conversion factors are involved, $n_{s,BET}$ may be best suited for
415 suspension measurements, and $n_{s,geo}$ may be best suited for dry-dispersed particle
416 measurements (Eqn. 3 to 4 or vice versa).

417 The usage of DLS-SSA for the calculation of S_{total}/M_{total} of suspension measurements
418 appears to be reasonable, as this leads to $n_{s,geo}$ for suspension measurements nearly equivalent
419 to $n_{s,geo}$ for dry-dispersed particles. When S_{total}/M_{total} is derived based on TSI-OPS
420 measurements, a value of $0.49 \text{ m}^2 \text{ g}^{-1}$ is obtained, which is smaller by a factor of about
421 thirteen compared to DLS-SSA. This difference may be mainly due to the fact that dry-
422 dispersed particles are typically prone to agglomeration (discussed below, i.e., Sect. 3.1)
423 compared to the measurements with suspended particles. The presence of fewer agglomerates
424 in suspended particles is shown in Fig. 1 of *Hiranuma et al.* (2014b). Since the size
425 distribution of a suspended sample for each experiment was not measured, DLS-SSA was
426 used for the data evaluation for suspension measurements throughout this study.

427 3. Results

428

429 3.1. Illite NX characterization

430

431 XRD results from the present and previous studies (*Friedrich et al.*, 2008; *Broadley et*
432 *al.*, 2012) of the major minerals in bulk samples of illite NX are presented in Table 2. The
433 results show that the bulk illite NX powder is composed of various minerals: illite, kaolinite,
434 quartz, calcite and feldspar, but the relative mass of these minerals for this study differs from
435 previous studies. For example, our measurement shows that the illite NX sample is composed
436 of ~69 wt% illite mineral, whereas others report a larger amount of illite from 74 to 86 wt%.
437 Similarly, we observed a somewhat different content of other minerals compared to previous
438 studies as listed in Table 2 (see also the Supplement Fig. S1). We note that the fractional
439 values in compositional fingerprints may deviate even within the same batch, as all three
440 XRD measurements deviated from the manufacturer's data (Table 2). Furthermore, our XRD
441 result indicates that the illite NX sample contains a smaller quartz fraction (3%) than IMt1-
442 illite from the Clay Mineral Society (10 to 15% quartz according to the official XRF data and
443 20% based on our own measurements).

444 To complement bulk XRD analysis, the abundances of thirteen elements (Pt, K, C, Ca,
445 O, Fe, Mg, Al, Si, P, S, Pb and Ti), which are commonly identified in illite rich samples, were
446 measured by EDX spectroscopy on a single particle basis. Four representative EDX spectra
447 are presented in Figure 1. The presence of Fe and Mg is typical and characteristic for illite NX
448 particles. The observed large amounts of Si and Al are due to the presence of layered
449 aluminosilicate structures (i.e., layer of SiO_2 and Al_2O_3). The observed dominant platinum
450 (Pt) signals in all spectra originate from the sputter coating conducted prior to EDX analyses.
451 Figure 1a shows the typical illite spectrum, which is similar to the one previously published in
452 *Welton* (1984). Illite rich minerals, which included impurities of calcite, TiO_2 and Pb-P, were
453 located by the brightness difference in the backscattered electron detector micrograph images.
454 The results are shown in Fig. 1b, c and d (inclusion of calcite, TiO_2 and Pb-P, respectively).
455 However, the EDX technique is not automated to detect these impurities present within the
456 illite NX particles because of their very small weight fraction. Therefore, the possible effect of
457 these observed impurities in illite NX upon the ice nucleation activity cannot be evaluated on
458 the basis of its bulk analysis of the chemical composition. Nonetheless, detection of non-illite

459 mineral components may reflect the complexities of natural dust particles, which typically
460 contain multiple sites with differing nucleation abilities. Thus, illite rich clay mineral can be
461 used as a reference material to mimic the ice nucleation activity of physically and chemically
462 complex natural dusts (Murray *et al.*, 2012).

463 The measured BET-SSA are 124.4 and 123.7 m² g⁻¹ with N₂ and H₂O vapor,
464 respectively, as the adsorbing gas on illite NX particle surfaces. The similar BET surface
465 areas for both N₂ and H₂O vapor gas adsorption suggest that the formation of a few
466 monolayers of H₂O does not alter the surface morphology or the mineralogical phase of illite
467 NX particles. For comparison, our measurements of θ_{N_2} for illite NX particles agreed with
468 previously reported data within 20% (104.2 m² g⁻¹; Broadley *et al.*, 2012). Since illite NX
469 particles have significant internal surface area, BET-derived surface areas can be expected to
470 be larger than those derived from the laser diffraction technique. Supporting this notion, an
471 SEM image of an illite NX particle from Broadley *et al.* (2012) shows how micron-sized
472 particles are made up of many nanometer-sized grains.

473 Normalized surface area distributions to the total surface area concentration measured
474 by four different techniques are shown in Fig. 2. According to the manufacturer, 95% (by
475 mass) of the dry and mechanically de-agglomerated illite NX particles have a diameter
476 smaller than 650 nm (i.e., D_{95}). This mass-based particle size is substantially smaller than that
477 of another type of Arginotec illite (Arginotec, SE-illite, $D_{95} = 5 \mu\text{m}$). Interestingly, all mass
478 size distributions measured in this study (not shown here) indicate a substantial mass fraction
479 above 650 nm which is, in all cases, larger than 5% (18%, 24%, 77% and 99.9% for DLS,
480 AIDA, MRI-DCECC and TSI-OPS for the FRIDGE immersion experiments, respectively),
481 indicating the presence of agglomerates in the aerosol and suspension phases prepared for the
482 IN experiments. The surface area distribution of the DLS hydrodynamic diameter-based
483 measurement (Fig. 2a) agreed well with *in situ* measurements from the AIDA chamber (Fig.
484 2b), suggesting the size distributions of dry illite NX particles during AIDA experiments were
485 similar to those of suspension measurements. This observation is consistent with results
486 presented in Hiranuma *et al.* (2014b). Briefly, the authors found agreement between the DLS-
487 based hydrodynamic diameter and the AIDA-derived volume equivalent diameter of hematite
488 particles. As opposed to the AIDA observation, the wider distributions and the shift in the
489 mode diameters in the MRI-DCECC measurements towards a larger size (0.62 μm , Fig. 2c)
490 when compared to Fig. 2a and b may indicate a higher degree of particle agglomeration as a
491 result of different degrees of pulverization during the particle generation processes or particle
492 coagulation at the high aerosol number concentration used for these measurements. A more

493 pronounced agglomeration effect was observed by the TSI-OPS measurements (Fig. 2d), such
 494 that a surface area distribution of supermicron-sized particles was obtained. Thus, different
 495 types of dry particle dispersion methods can contribute to varying degrees of agglomeration
 496 and the observed differences in surface area distributions. Though all size segregating
 497 instruments used in the present study are well calibrated, we cannot rule out the effect of
 498 measurement techniques themselves on the observed differences in particle size distribution.
 499 In Sect. 4.4 we discuss whether agglomeration has an effect on the IN activity.

500 The cation release by illite NX in the aqueous suspension was measured with IC as a
 501 function of time. The suspension was kept mechanically agitated for three weeks. The
 502 following cations were identified in the samples: K^+ , Ca^{2+} and Mg^{2+} . As seen in Fig. 3, IC
 503 data clearly demonstrates that roughly all cations were released into the aqueous environment
 504 by illite NX almost instantaneously. The concentration of the cations increased rapidly and
 505 reached equilibrium within the first 2 min after immersion of sample into water. Of all the
 506 cations measured, only Ca^{2+} exhibited a slow concentration raise on the longer time scales.

507

508 3.2. Immersion freezing measurements and inter-comparisons

509

510 All ice nucleation spectra with $n_{s,BET}(T)$ and $n_{s,geo}(T)$ are shown in Figs. 4 and 5,
 511 respectively. A similar figure with $n_m(T)$ is also shown in the Supplement Fig. S2.
 512 Furthermore, we compare the n_s data from seventeen instruments to four literature results.
 513 Specifically, IN spectra reference curves of previously reported illite NX particles (*Broadley*
 514 *et al.* 2012, hereafter B12), microcline particles (*Atkinson et al.*, 2013, hereafter A13), ATD
 515 and desert dusts (*Niemand et al.*, 2012, hereafter N12) are also expressed as both $n_{s,BET}(T)$ and
 516 $n_{s,geo}(T)$. The conversion between $n_{s,geo}(T)$ and $n_{s,BET}(T)$ was performed according to Eqns. 3
 517 and 4. The $n_s(T)$ (m^{-2} as a function of $^{\circ}C$) fits from the reference literature are:

518

$$519 \quad n_{s,BET}^{A13} = 10^4 \times \exp(-1.038(T - 273.150) + 275.260) \quad (5)$$

$$520 \quad n_{s,BET}^{B12} = 10^4 \times \exp[(6.530 \times 10^4) + ((-8.215 \times 10^2) \times (T - 273.150)) +$$

$$521 \quad (3.447 \times (T - 273.150)^2) + ((-4.822 \times 10^{-3}) \times (T - 273.150)^3)] \quad (6)$$

$$522 \quad n_{s,geo}^{N12(ATD)} = \exp(-0.380T + 13.918) \quad (7)$$

$$523 \quad n_{s,geo}^{N12(Dust)} = \exp(-0.517T + 8.934). \quad (8)$$

524

525 For microcline (K-feldspar), the $n_{s,geo}$ to $n_{s,BET}$ conversion was performed using a laser
526 diffraction-based surface-to-mass conversion factor of $0.89 \text{ m}^2 \text{ g}^{-1}$ and an N_2 BET-SSA of 3.2
527 $\text{m}^2 \text{ g}^{-1}$ (Atkinson *et al.*, 2013). For ATD and natural dust, we used a surface-to-mass
528 conversion factor of $3.6 \text{ m}^2 \text{ g}^{-1}$, assuming a monodisperse particle size at the lognormal fit
529 mode diameter of $0.64 \text{ }\mu\text{m}$ (Niemand *et al.*, 2012) and the measured N_2 BET-SSA of 34.4 m^2
530 g^{-1} (*this study*). We note that the ATD parameterization is valid only for $-26.7 \text{ }^\circ\text{C} < T < -17.7$
531 $^\circ\text{C}$. In addition, we also present 14, 0.14 and 0.0014% scaled A13 n_s curves to see if K-
532 feldspar (microcline) can be used as a scaling factor to determine the $n_s(T)$ of illite NX.

533 We do not attempt to completely discuss the immersion freezing activity of illite NX
534 particles measured by each measurement technique. Instead, brief remarks regarding each
535 method are summarized below. The detailed discussion of the methods inter-comparison
536 follows in Sect. 3.3.

537 **3.2.1. BINARY:** This recently developed microliter droplet assay technique
538 demonstrated its capability of measuring immersion freezing of clay minerals in the
539 temperature range of -15 to $-24 \text{ }^\circ\text{C}$. Similar to most of the other suspension-based techniques,
540 BINARY identified a steep $n_s(T)$ increase, which started just below $-20 \text{ }^\circ\text{C}$. The BINARY
541 $n_s(T)$ spectrum was derived by compiling measurements with varied illite NX mass
542 concentrations over two orders of magnitude (0.1 to 10 mg mL^{-1} , see the Supplementary
543 Methods). Immersion freezing efficiency of illite NX particles collapsed into a single $n_s(T)$
544 spectrum, i.e. IN efficiency does not depend on suspended particle mass for the concentration
545 range studied here. This observation is a check for consistency and it implies that ice
546 nucleation is indeed triggered by suspended illite NX particles, and neither by impurities
547 contained in the water used for dilution nor at the glass surface supporting the droplets. If IN
548 efficiency did depend on suspended particle mass, different $n_s(T)$ spectra would result from
549 the various illite NX concentrations, which are shifted by the respective dilution factor.

550 **3.2.2. CSU-IS:** This new immersion freezing device was used to investigate the
551 freezing activity of both bulk suspension and size-segregated particles in suspension. A new
552 approach was employed for size-selected measurements, wherein 500 nm mobility diameter
553 size-selected particles were collected on a Nuclepore filter and then rinsed from it for the
554 immersion freezing measurements. The results suggest size independence of n_s within the
555 experimental uncertainties (a combination of binomial sampling error and the uncertainty of
556 conversion of aerodynamic particle diameter to mass) for the range of examined size (500 nm
557 vs. bulk) and mass concentrations of bulk illite NX powder in suspensions from 3.1×10^{-6} to

558 0.5 wt%, for non-size-segregated particles, and 2.2×10^{-5} to 4.4×10^{-4} wt% for size-
559 segregated particles.

560 **3.2.3. Leeds-NIPI:** This suite of cold stage instruments has the capacity to operate
561 using droplets with volumes in the microliter to picoliter range. This enables high resolution
562 immersion freezing analysis for a wide range of temperatures from higher ($-22 \text{ }^\circ\text{C} < T < -11$
563 $^\circ\text{C}$) to lower temperatures ($-37 \text{ }^\circ\text{C} < T < -26 \text{ }^\circ\text{C}$). The highest freezing temperatures are
564 attained with the largest droplets, which contain the largest surface area of illite NX.
565 Combined with the previous parameterization reported in *Broadley et al. (2012)*, the Leeds-
566 NIPI data follows the overall $n_s(T)$ spectrum defined by the bulk of the instruments. This
567 suggests that immersion freezing efficiency, inferred by $n_s(T)$, of illite NX particles is
568 dependent on neither droplet volume nor mass of illite NX particles in suspension (i.e., wt%
569 0.1 or 1%); instead the freezing efficiency only depends on the surface area per droplet.
570 Together with CSU-IS, these two instruments provided data points for temperature as high as
571 $\sim -11 \text{ }^\circ\text{C}$, estimating a similar lower-limit of $n_{s,\text{BET}}$ values of $\sim 10 \text{ m}^{-2}$.

572 **3.2.4. M-AL and M-WT:** Both methods examine individual drops that are freely
573 suspended without any contact with walls or substrates. In M-WT drops are floated at their
574 terminal velocities in a laminar air stream, in which conditions of ventilation and heat transfer
575 are similar to those of droplets falling through the atmosphere. Both M-AL and M-WT
576 techniques analyzed the freezing efficiency of drops containing polydisperse illite NX
577 particles in the temperature range between -14 and $-26 \text{ }^\circ\text{C}$. The n_s values agree reasonably
578 well with substrate-supported suspension experiments (with the exception of FRIDGE
579 experiments), implying that the surface making contact with the substrate has a negligible
580 effect on immersion freezing for our experimental conditions.

581 **3.2.5. NC State-CS:** Extensive experimental conditions were realized by NC State-CS
582 (*Wright and Petters, 2013; Hader et al., 2014*). Unique aspects of this instrument are the
583 sampling of drops within a squalene oil matrix that allows for experiments using cooling rates
584 as slow as 0.01 K min^{-1} and an automated freeze detection algorithm that allows rapid
585 processing of more than 1,000 drops per experiment to improve sample statistics. Drops
586 containing ~ 0.0001 to 1.0 wt% of the illite NX test sample were studied at a cooling rate of 1
587 K min^{-1} to find the immersion freezing ability. A total of nine immersion mode freezing
588 experiments, spanning a range of drop volumes from ~ 400 picoliter to 150 nanoliter, were
589 performed. Using this instrument a wide range of temperatures was investigated ($-34 \text{ }^\circ\text{C} < T <$
590 $-14 \text{ }^\circ\text{C}$) yielding $n_s(T)$ values ranging from 10^2 to 10^{10} m^{-2} . The data from the nine individual
591 runs collapsed into a single $n_s(T)$ spectrum suggesting that the mass loading of dust in the

592 drop did not affect the measurements for the wt% values investigated. At the high T end ($T > -$
593 $20\text{ }^{\circ}\text{C}$), the data are in reasonable quantitative agreement with the CSU-IS measurements. At
594 the low T end ($T < -20\text{ }^{\circ}\text{C}$), the data are in agreement with the B12 reference spectrum.

595 **3.2.6. CU-RMCS:** The University of Colorado (CU)-RMCS examined the freezing
596 abilities of droplets containing 1.0 wt% illite NX. CU-RMCS detected the warmest immersion
597 freezing of illite NX particles at about $-23\text{ }^{\circ}\text{C}$ under the experimental conditions used in the
598 present work (see the Supplementary Methods for further details). Results for $-32\text{ }^{\circ}\text{C} < T < -$
599 $23\text{ }^{\circ}\text{C}$ are from six different experiments using four different droplet size bins: 10-20 μm , 20-
600 60 μm , 60-120 μm , and 120-200 μm (lateral diameter). These droplet sizes correspond to a
601 variation in droplet volume from ~ 0.3 picoliter to 2.5 nanoliter.

602 **3.2.7. AIDA:** The AIDA cloud simulation chamber generates atmospherically relevant
603 droplet sizes (several μm in diameter, varying with cooling rates), and therefore closely
604 simulates mixed-phase cloud conditions. Ice-nucleating efficiencies of both polydisperse and
605 quasi-monodisperse illite NX particles were investigated in this study. n_s of DMA size-
606 selected illite NX particles (200, 300 and 500 nm mobility diameter) agreed well with that of
607 the polydisperse population for immersion freezing experiments, within previously reported
608 uncertainties ($T \pm 0.3\text{ }^{\circ}\text{C}$ and $n_s \pm 35\%$; *Steinke et al.*, 2011). Thus, a negligible size
609 dependency of n_s for ‘submicron’ dry illite NX particles for temperatures below $-27\text{ }^{\circ}\text{C}$ was
610 found. Previously, *Hiranuma et al* (2014a) demonstrated the size independence of the n_s value
611 using two different sizes of submicron hematite particles (200 and 1000 nm volume
612 equivalent diameter) based on AIDA deposition mode nucleation experiments. Such a
613 similarity might remain true for the immersion mode freezing of mineral dust particles that are
614 smaller than 1 μm diameter.

615 **3.2.8. CSU-CFDC:** This CFDC provided data for condensation/immersion freezing at
616 around -21.2 , -25.1 and $-29.7\text{ }^{\circ}\text{C}$ (a total of eight data points with two, two and four points at
617 around each temperature, respectively), which extends to a warmer region than the AIDA
618 measurements. As demonstrated in *DeMott et al.* (2014), higher RH_w values were required for
619 full expression of immersion freezing in CSU-CFDC. The use of 105% RH_w in CSU- CFDC
620 does not capture INP activity for many natural dusts, up to a factor of three INP activities.
621 Comparably, the CSU-CFDC results agreed well with the AIDA measurements within a
622 factor of three in $n_{s,\text{geo}}$ estimation (AIDA $n_s >$ CSU-CFDC n_s ; *DeMott et al.*, 2014). All the
623 CFDC measurements were conducted with 500 nm mobility diameter size-selected particles,
624 as discussed in the Supplementary Methods.

625 **3.2.9. EDB:** With EDB, both the contact and immersion mode freezing efficiencies of
626 illite NX particles were investigated. The contact nucleation mode n_s were clearly higher than
627 the immersion mode n_s (by more than one order of magnitude in terms of $n_{s,geo}$, Fig. 5i). This
628 was in part due to the fact that immersion freezing experiments were conducted only when
629 illite NX particles were not frozen via contact nucleation but remained immersed in a
630 supercooled droplet in the EDB cell (see the Supplementary Methods).

631 **3.2.10. FINCH:** The immersion freezing results from FINCH showed the highest n_s
632 values in the -22 to -27 °C temperature range out of all of the other instrument results. All the
633 FINCH measurements were conducted with 500 nm mobility diameter size-selected particles.
634 Two possible reasons for high n_s values when compared to the other measurements are: 1) an
635 overestimation of n_s due to excess N_{ice} and/or underestimated S_{total} or 2) a large temperature-
636 uncertainty. It is noteworthy that the total INP concentration was kept below 140 L⁻¹ in order
637 to avoid saturation limitation due to a high number of growing ice crystals (*DeMott et al.*,
638 2011). A constant total concentration of particles continuously passing through the chamber
639 was maintained at $1.07 \pm 0.17 \text{ cm}^{-3}$ (average \pm standard deviation).

640 **3.2.11. FRIDGE:** FRIDGE data, which cover both measurements of dry and
641 immersed particles with the same instrument but with different sample processing, lie within
642 the upper edge of the bulk of other n_s data points. There are a few important implications from
643 the FRIDGE results. First, on average, the measurements with dry particles in the ‘default’
644 setting showed more than an order of magnitude higher n_s in comparison to the immersed
645 particles in FRIDGE experiments (both $n_{s,BET}$ and $n_{s,geo}$, Figs. 4 and 5) at $-25 \text{ °C} < T < -18 \text{ °C}$.
646 For instance, FRIDGE experiments in the pure immersion mode showed much lower n_s than
647 that with the default setting (i.e., combined deposition and immersion mode), but agreed with
648 other immersion datasets. Second, a sudden increase in $n_s(T)$ was found for the measurements
649 with immersed particles at $\sim -20 \text{ °C}$, suggesting a dominant activation around -20 °C. This
650 transition is a unique behavior only found with the FRIDGE’s IN detecting sensitivity. A
651 temperature shift (i.e., shifting the data $\sim 7 \text{ °C}$ lower) results in FRIDGE data overlapping with
652 the bulk of other data and may offset discrepancies. However, other mechanistic
653 interpretations (e.g., contribution of agglomeration) are also plausible causes of this
654 discrepancy. More detailed discussions of the role of agglomerates upon n_s and sample
655 processing are available in Sect. 4.4 and 4.5.

656 **3.2.12. LACIS:** With the shortest instrument residence time ($\sim 1.6 \text{ s}$), LACIS measured
657 immersion mode freezing of illite NX particles for three different mobility diameters (300,
658 500 and 700 nm) from -31 °C down to the homogeneous freezing temperature. Similar to

659 AIDA results, a size independence of n_s of submicron illite NX particles was observed within
660 defined experimental uncertainties (see the Supplementary Methods). Further, without any
661 data corrections, the results of LACIS reasonably agreed with AIDA measurements.
662 Furthermore, though there is no overlapping temperature range for LACIS and CSU-CFDC in
663 the present study, consistency between data from LACIS and CSU-CFDC for other clay
664 minerals (i.e., different kaolinite samples) has been described previously (Wex *et al.*, 2014).
665 The results from both instruments agreed well with each other from a data evaluation based on
666 n_s , and this agreement was even improved when the different residence times in LACIS and
667 the CSU-CFDC were accounted for (i.e., when nucleation rate coefficients were compared).
668 Furthermore, a size independence of the immersion mode freezing was seen for Fluka-
669 kaolinite particles with mobility diameters of 300 and 700 nm in Wex *et al.* (2014), and for
670 illite NX particles when comparing particles with mobility diameters of 500 nm to bulk
671 material (Augustin-Bauditz *et al.*, 2014).

672 **3.2.13. MRI-DCECC:** Comparison between polydisperse and size-selected (300 nm
673 mobility diameter) measurements in this cloud simulation chamber demonstrated the size
674 independency of n_s for submicron illite NX particles for slightly higher temperatures (up to -
675 21 °C) than AIDA results. Interestingly, MRI-DCECC data exhibited at least an order of
676 magnitude higher n_s values than most other suspension measurements. We note that only
677 negligible freezing events were detected above -21 °C even with a $\sim 9000 \text{ cm}^{-3}$ number
678 concentration of polydisperse illite NX particles in part due to the detection limit of the welas
679 optical counter of $N_{\text{ice}} = 0.1 \text{ cm}^{-3}$.

680 **3.2.14. PINC:** PINC provided data for immersion freezing at around -25.4, -30.2 and -
681 34.6 °C (a total of nine data points with one, four and four points at around each temperature,
682 respectively). The estimated n_s values are in agreement with other measurements for the test
683 range of $-35 \text{ °C} < T < -25 \text{ °C}$ after applying a residence time correction of about a factor of
684 three. The data are for ice nucleation onto 500 and 1000 nm mobility diameter illite NX
685 particles; therefore, an OPC threshold size of 2 μm for ice detection is used. The impactor
686 used for sampling particles into PINC was characterized for size-resolved particle losses and
687 was found to have a cutoff (D_{50}) of 725 nm mobility diameter. As such, when determining
688 $n_{s,\text{geo}}$ the particles losses (25 to 60%, see the Supplementary Methods for more details) were
689 taken into account for calculating activated fractions. We note that $n_{s,\text{geo}}$ increased after
690 adjusting the data, resulting in agreement between the data from PINC and data from LACIS,
691 AIDA and UC-RMCS in the temperature range from -25 to -35 °C.

692 **3.2.15. PNNL-CIC:** The IN efficiency of illite NX particles in the immersion mode in
693 the temperature range of $-35\text{ }^{\circ}\text{C} < T < -27\text{ }^{\circ}\text{C}$ was observed to increase at lower temperatures.
694 Estimated n_s values were somewhat higher in this temperature range when compared to those
695 from most of the other measurements. Data were obtained at conditions where PNNL-CIC
696 was operated at 105% RH_w at three different temperatures. Dust particles greater than $\sim 1\text{ }\mu\text{m}$
697 (50% cut size) were removed before they were size-selected and transported to the PNNL-
698 CIC. The OPC detection threshold was set $\geq 3\text{ }\mu\text{m}$; see the Supplementary Methods for more
699 details.

700 **3.2.16. IMCA-ZINC:** Coupled with IMCA, ZINC showed reasonable agreement with
701 AIDA and PNNL-CIC. This reproducibility verified the performance of the IMCA-ZINC
702 combination, which was not tested during ICIS-2007 (*DeMott et al.*, 2011), perhaps due to the
703 similarity in the experimental conditions (i.e., particle generation) to the other two methods.
704 We also note that the residence time in ZINC is about a factor of three longer than that in
705 PINC. The IMCA-ZINC measurements in comparison to the measurements with ZINC alone
706 (i.e., a combination of deposition nucleation, contact-, condensation-, surface condensation-
707 and immersion freezing) is discussed in Sect. 4.5 in more detail.

708 Overall, as described above (Sects. 3.2.1 to 3.2.6), suspension experiments with cold
709 stage devices and levitation techniques provide IN measurements under more controlled (with
710 respect to droplet size, concentration and mass of particles) conditions and a wider
711 temperature range (up to $-11\text{ }^{\circ}\text{C}$) than comparable dry-dispersed particle experiments. The
712 resulting n_s values from these suspension experiments are also independent of the total
713 number of droplets and suspended dust particle mass.

714 The estimated n_s values of dry test particles below $-25.5\text{ }^{\circ}\text{C}$ are in reasonable
715 agreement with a previous study (*Broadley et al.*, 2012) at temperatures below $-25\text{ }^{\circ}\text{C}$.
716 Furthermore, the strong temperature dependence and size independence of n_s may suggest a
717 uniform distribution of freezing sites over the total surface of illite NX particles in the
718 immersion mode in this temperature range. Specifically, AIDA and MRI-DCECC have shown
719 size-independent n_s values for submicron dry-dispersed particles. Overall, compared to
720 suspension measurements, dry-dispersed particle measurements showed higher n_s values. For
721 example, FINCH is the only instrument which showed higher n_s values than the
722 parameterization by *Niemand et al.* (2012) for ATD. Likewise, AIDA results indicated
723 slightly higher n_s values than CSU-CFDC's results. The lower n_s of CSU-CFDC may be a
724 consequence of underestimation of N_{ice} , possibly due to its constrained RH_w (at 105%) and/or
725 the disturbance of aerosol lamina between two plates in a CFDC (*DeMott et al.*, 2014).

726 3.3. Inter-comparisons based on the slope parameter of $n_s(T)$ spectra

727

728 A compilation of seventeen n_s spectra from seventeen instruments in a temperature
729 range between -10.1 and -37.5 °C is presented in Fig. 6. For both the geometric area-based
730 and the BET area-based n_s , the differences among measurements can be more than one order
731 of magnitude at any given temperature. Diversity is especially pronounced for several orders
732 of magnitude in n_s at $-27\text{ °C} \leq T \leq -18\text{ °C}$, where the results from suspension measurements
733 and a majority of dry measurements coexist (see the investigated T range for each technique in
734 Table 1). Another notable feature of this specific temperature range in Fig. 6 is the
735 coincidence of the steepest slope in the spectrum (i.e., the absolute value of $\Delta\log(n_s)/\Delta T$ in \log
736 $\text{m}^{-2}\text{ °C}^{-1}$, hereafter denoted as $\Delta\log(n_s)/\Delta T$) when compared to other temperature ranges. For
737 instance, n_s increases sharply at temperatures colder than -18 °C to be nearly parallel to the
738 A13 parameterization down to -27 °C, where it starts leveling off and is eventually
739 overlapping with the N12 parameterization at the low temperature segment.

740 Correspondingly, the overall trend of the spectrum is traced by the measurements from
741 NC State-CS alone (Fig. 4e). Moreover, the slopes of the spectrum for three sub-segments ($-$
742 $34\text{ °C} < T < -27\text{ °C}$, $-27\text{ °C} < T < -20\text{ °C}$, and $-20\text{ °C} < T < -14\text{ °C}$) can be calculated from
743 interpolated data and compared to N12 and A13 parameterizations. As expected, the steepest
744 slope in the spectrum (= 0.66) of the NC State-CS data was found in the $-27\text{ °C} < T < -20\text{ °C}$
745 range, which was similar to that of the A13 parameterization (0.45 for $T > -25\text{ °C}$). However,
746 smaller slope values are found for the other two segments (0.18 for $T < -27\text{ °C}$ and 0.29 for T
747 $> -20\text{ °C}$), which are comparable to the temperature-independent N12 slopes (0.17 for ATD
748 and 0.22 for Dust) and the B12 slope (0.25 for $-35\text{ °C} < T < -27\text{ °C}$), suggesting that a
749 dominant fraction of INP contained in our test dust becomes ice active in immersion freezing
750 at $-27\text{ °C} < T < -20\text{ °C}$. In addition, FRIDGE immersion mode measurements also show a
751 sharp decrease in $\Delta\log(n_s)/\Delta T$ (from 0.59 to 0.25, Figs. 4k and 5k) for the measurements with
752 immersed particles at $\sim -20\text{ °C}$. Similar observations are made by most of the other suspension
753 measurement techniques. In short, most suspension methods capture the steepest segment of
754 the $n_s(T)$ spectral slopes ($\Delta\log(n_s)/\Delta T$) at $-27\text{ °C} < T < -20\text{ °C}$, where the slope is nearly
755 parallel to the A13 parameterization. One exception is CU-RMCS (Fig. 4f). The highest
756 possible freezing temperature investigated by this experimental system was about -23 °C with
757 ~ 2.5 nanoliter droplets containing 1.0 wt% illite NX (see the Supplementary Methods).
758 Hence, CU-RMCS did not capture the transition in $\Delta\log(n_{s,BET})/\Delta T$ at around -20 °C, but the
759 steep slope of the spectrum (= 0.36) validated the high density of IN active sites below -23 °C.

760 The error in temperature for this technique is always ± 0.5 °C, based on freezing experiments
761 without any foreign substances in supercooled drops (i.e., homogeneous freezing
762 experiments).

763 Similarly, dry-dispersed particle measurements also exhibit scattered data for their
764 measured temperature ranges. Both agreements and equally important disagreements were
765 observed. First, the agreements are summarized. AIDA data show that the values of
766 $\Delta\log(n_{s,geo})/\Delta T$ ($= 0.22$, Fig. 5g) are identical for both polydisperse and size-selected
767 measurements, perhaps suggesting a uniform distribution of active sites over the available
768 S_{total} of illite NX in this study. Similarly, IMCA-ZINC's $\Delta\log(n_{s,geo})/\Delta T$ ($= 0.24$, Fig. 5p)
769 derived from 200, 400 and 800 nm mobility diameters is virtually identical to the slope
770 estimated from AIDA measurements. PINC estimated $\Delta\log(n_{s,geo})/\Delta T$ ($= 0.26$, Fig. 5n) values
771 are in reasonable agreement with AIDA and IMCA-ZINC and N12 parameterizations at
772 temperatures below -25 °C. From the CSU-CFDC results, $\Delta\log(n_{s,geo})/\Delta T$ derived from
773 interpolated data is 0.40 (Fig. 5h). Considering the AIDA and CSU-CFDC data, the $n_s(T)$
774 spectrum depicts similar trends (i.e., n_s or temperature deviation around -27 °C) compared to
775 those seen in the NC State-CS results (Fig. 5e) and is also parallel to the A13 curve (slope =
776 0.45) down to temperatures around -27 °C and is parallel to the N12 Dust curve (slope = 0.22)
777 for the lower temperature segment. LACIS measurements show that $\Delta\log(n_{s,geo})/\Delta T$ ($= 0.19$,
778 Fig. 5l) is also in agreement with that from AIDA, verifying a deteriorated freezing ability of
779 illite NX particles in the investigated temperature range. EDB was used to examine both the
780 contact and immersion freezing modes. Nonetheless, the slopes of the spectra for both modes
781 (0.11 for immersion mode freezing and 0.16 for contact mode freezing, Fig. 5i) are similar to
782 the N12 ATD curve (slope = 0.17). From the fact that the value of $\Delta\log(n_{s,geo})/\Delta T$ of FINCH
783 ($= 0.27$, Fig. 5j) above -27 °C is similar to that of the N12 dust parameterization (whereas this
784 relationship would be expected below -27 °C), we suspect that a temperature uncertainty may
785 be the main cause of the observed deviation of its data from others. Lastly, at -35 °C $< T < -27$
786 °C, PNNL-CIC's $\Delta\log(n_{s,geo})/\Delta T$ ($= 0.19$, Fig. 5o) agreed well with that of the N12 dust
787 parameterization in the same temperature range.

788 Next, the disagreements between dry-dispersed particle and suspension measurements
789 are discussed. Specifically, the MRI-DCECC results show lower values of $\Delta\log(n_{s,geo})/\Delta T$ ($=$
790 0.29) up to -21 °C as compared to the suspension measurements. Additionally, in the
791 temperature range from -29 °C $< T < -21$ °C, the MRI-DCECC data show higher values of n_s
792 than those observed in suspension measurements. This relatively constant $\Delta\log(n_s)/\Delta T$ value
793 along with higher n_s values through the range contrasts with the observed sharp transition in

794 $\Delta \log(n_s)/\Delta T$ in suspension measurements. We note that MRI-DCECC experiments may have
795 been carried out in the presence of a high degree of agglomeration (Fig. 2c and d). Hence,
796 particle processing (i.e., drying and suspension) may not be the only factor causing this
797 difference and other contributions cannot be ruled out (see Sect. 4).

798 To conclude, the results from suspension and dry measurements suggest evidence that
799 the n_s of illite NX particles derived from immersion freezing is independent of or only weakly
800 dependent on droplet size, mass percent of illite NX sample in suspension and droplets,
801 particle size of the tested illite NX and cooling rate during freezing in the range of conditions
802 probed; see the Supplementary Methods for more detailed information regarding experimental
803 conditions for each instrument. Overall, the sample-processing (i.e., dry vs. suspension
804 sample) may have an effect on the immersion freezing efficiency of illite clays. A more
805 detailed discussion will follow in Sect. 4 below.

806 4. Discussion

807

808 For detailed comparison of methodologies, the immersion freezing properties of illite
809 NX particles in a wide range of temperatures is further discussed by comparing $n_s(T)$ spectra
810 from all seventeen instruments (Sect. 4.1). Specifically, we present T -binned average data
811 (i.e., 1 °C bins for $-37\text{ °C} < T < -11\text{ °C}$). A moving average (where original data points are finer
812 than 1 °C) or a Piecewise Cubic Hermite Interpolating Polynomial function (where original data
813 points are coarser than 1 °C) was used for data interpolation. All data from the seventeen
814 instruments, as shown in Figs. 4 and 5, were interpolated.

815 We also discuss potential reasons for the diversity observed from inter-comparisons of
816 dry and suspension measurement techniques. Both systematic errors (Sect. 4.2) and
817 mechanistic uncertainties (Sect. 4.3 to 4.6) are qualitatively evaluated to understand the
818 measurement uncertainties of such techniques. Some factors may introduce diversity in n_s ,
819 whereas others may shift activation temperatures horizontally to match the n_s values from
820 other instruments, perhaps biasing the overall accuracy and precision of instruments. Here we
821 address the relative importance of those factors with respect to their effect on the estimation of
822 n_s .

823

824 4.1. Dry vs. suspension $n_s(T)$ data

825

826 The multiple exponential distribution fits (also known as the Gumbel cumulative
827 distribution function) for T -binned data are shown in Fig. 7. The fits for T -binned maxima and
828 minima n_s from seventeen measurement techniques are presented as pink shaded areas. All
829 fits presented in this figure are derived using parameters shown in Table 3. As can be inferred
830 from the table, a higher correlation coefficient (r) was found when inter-comparing the
831 suspension measurements as compared with inter-comparing the dry-dispersed methods,
832 suggesting reasonable agreement and consistency for the results from immersion freezing
833 studies with suspensions. Interestingly, a higher r for $n_{s,\text{geo}}$ than $n_{s,\text{BET}}$ was found for dry-
834 dispersed particle measurements as compared to the suspension measurements. The use of
835 more conversion factors to estimate $n_{s,\text{BET}}$ (i.e., from Eqn. 3 and 4) may introduce
836 uncertainties and discrepancies between these measurement techniques. It is also noteworthy
837 that the T -binned ensemble maximum and minimum values are largely influenced by dry-

838 dispersed particle and suspension results, respectively, implying the previously discussed
839 discrepancy between these two techniques.

840 It is observed that the largest deviation between the maxima and minima in the
841 horizontal and vertical axes, corresponding to $\text{Hor}_{\text{Max-Min}}$ and $\text{Ver}_{\text{Max-Min}}$, respectively, shown
842 in Fig. 7, is similar for both $n_{s,\text{BET}}$ (Fig. 7a) and $n_{s,\text{geo}}$ (Fig. 7b). Nevertheless, $n_{s,\text{BET}}$ is
843 representative of measurements with suspended samples because fewer corrections and
844 assumptions are involved for its estimation when compared to that with dry-dispersed
845 particles. Hence, $n_{s,\text{BET}}$ may be a good proxy for comparing IN efficiencies of dust particles
846 from various instruments. We also report the absolute values of $\Delta\log(n_s)/\Delta T$ for four T -
847 segregated segments based on T -binned Lin. Avg. (multiple exponential distribution fit to the
848 T -binned average data in the linear space), T -binned Max. (fit to the T -binned maxima in the
849 linear space) and T -binned Min. (fit to the T -binned minima in the linear space) in Fig. 7 (i.e.,
850 T_1 to T_4). The slopes are comparable to the slope of the A13 parameterization in the T_1 to T_3
851 segments (-11 to -27 °C), while the slope in the T_4 segment is similar to those of the N12
852 parameterizations. These results are consistent with the results described in Sect. 3.3. Further,
853 $\text{Ver}_{\text{Max-Min}}$ for roughly three orders of magnitude with respect to n_s is observed in a
854 temperature region around ~ -20 °C for both $n_{s,\text{BET}}(T)$ and $n_{s,\text{geo}}(T)$ spectra. Such high n_s
855 variability was expected due to the contribution from MRI-DCECC, FINCH and FRIDGE
856 measurements, which may have influenced the overall fit in that temperature range. Likewise,
857 our $\text{Hor}_{\text{Max-Min}}$ shows that the seventeen measurements are in reasonable agreement within 7.8
858 °C (-36.8 °C, -33.0 °C, -29.0 °C (*min, log fit, max*)) at $n_{s,\text{BET}}$ of $5.2 \times 10^9 \text{ m}^{-2}$ and 7.5 °C (-36.7 °C, -
859 32.8 °C, -29.2 °C (*min, log fit, max*)) at $n_{s,\text{geo}}$ of $1.5 \times 10^{11} \text{ m}^{-2}$.

860 T -binned $n_{s,\text{BET}}(T)$ and $n_{s,\text{geo}}(T)$ spectra are presented in Fig. 8a and b, respectively. In
861 this figure, panels i, ii and iii show T -binned data averaged in the linear space of all seventeen
862 instruments, all suspension type measurements, and all measurements that involved dry
863 particles, respectively, while panel iv shows a comparison between suspension and dry-
864 particle measurements. We note that the data from ‘EDB (contact)’ and ‘ZINC’ (Welti *et al.*,
865 2009) were not used for generating T -binned data since our focus was on immersion mode
866 freezing. We also note that the n_s results from nine IN measurement techniques provide n_s
867 data at -23 °C and -24 °C, where we find an abrupt increase in $\Delta\log(n_s)/\Delta T$ and n_s deviations.
868 Investigated T ranges for each instrument are listed in Table 1.

869 As described in Sect. 3.2, suspension measurements possess sensitivity at high
870 temperatures (up to -11 °C), indicating that their ability to control the concentration or dilution
871 of suspension over a wide range is of great advantage in detecting rare INPs. Moreover,

872 suspension experiments with small picoliter or nanoliter droplets allow measurements right
873 down to the homogeneous freezing limit (~ -37 °C; *Koop et al.*, 2000). In turn, suspension
874 methods with microliter droplets may run into ‘background problems’ at temperatures below
875 about -20 °C to -25 °C for samples that do not contain many IN active at these temperatures,
876 because then impurities contained in the water may trigger freezing. Conversely, dry aerosol
877 methods lack sensitivity for detecting rare IN at high temperatures because of their low
878 sample volume. These dry particle measurements are in general good for low temperature
879 measurements, where the number of particles nucleating ice increases and instruments have
880 higher ice detection efficiencies. For temperatures below -27 °C, our T -binned fits exhibit a
881 reasonable agreement with the suspension experiments reported by *Broadley et al.* (2012).
882 Furthermore, dry-dispersed particle measurements show higher n_s values when compared to
883 suspension measurements above about -27 °C (Fig. 8iv). We will discuss possible
884 explanations for the observed diversity of data from different techniques in detail below.

885 In addition, T -binned $n_{s,BET}(T)$ and $n_{s,geo}(T)$ spectra averaged in the log space are
886 presented in Fig. S3. Similarly, we also present T -binned ratios of the individual
887 measurements to the log fit of the data [All (log), Sus (log) or Dry (log) from Table 3] across
888 the temperature range covered for all the measurement techniques (-37 °C $< T < -11$ °C) in the
889 Supplement Figs. S4-S8. These figures provide inter-comparisons of the n_s deviations across
890 the various techniques employed in this study.

891

892 4.2. Limitations of instrument types

893

894 Groups participating in this study used different experimental setups to measure
895 immersion freezing efficiencies of illite NX test samples. As a consequence, various
896 experimental procedures, such as particle generation, particle size-segregation, S_{total}
897 estimation, ice crystal detection or counting, ice crystal detection size limits for OPCs or
898 CCDs, and particle loss at the inlet and/or in the chamber can potentially yield substantial
899 systematic uncertainties in the estimation of n_s . Below we qualitatively discuss potential errors
900 and limitations involved in each instrument-type (cold stage, levitator, CECC and CFDC).

901 Limitations of substrate-supported optical microscopy and cold stage experimental
902 setups may come from inhomogeneous cooling of the substrate and the surrounding media,
903 the effects of RH changes surrounding the drops for non-substrate-supported cold stage
904 setups, potential contamination during sample preparation and measurements (e.g., particle

905 processing in a solvent) and/or uncontrollable heat transfer between the cold plate surface and
906 the particle substrate (e.g., FRIDGE).

907 Levitator techniques require extensive pre-characterization of physico-chemical
908 properties. Furthermore, since the overall system characterization is more complex and labor
909 intensive, only specific subsets (i.e., suspended samples or reference particles) can be
910 examined using this method.

911 The development of AIDA-CECC allows the simulation of atmospherically
912 representative cloud parcel formation and evolution (*Möhler et al.*, 2003). Therefore, it is an
913 advantage of CECC that the parameterization derived from its experiments can be most
914 readily extended to atmospheric conditions (*Niemand et al.*, 2012). Development of large (up
915 to 84 m³, i.e., AIDA) and/or temperature-controlled dynamic cloud simulation chambers (e.g.,
916 MRI-DCECC; *Tajiri et al.*, 2013, a design which follows from *DeMott and Rogers*, 1990)
917 enabled the exploration of heterogeneous ice nucleation properties of typical particulate
918 samples in a wide range of particle concentrations, temperatures ($-100\text{ °C} < T < 0\text{ °C}$), cooling
919 rates and nucleation times. However, the utilization of such an instrument to correctly
920 measure the totality of INPs with a reasonable detection sensitivity ($<0.1\text{ L}^{-1}$), both in the lab
921 and field settings, has not yet been realized due to CECC's limitations. These limitations
922 include ice losses by settling (e.g., *DeMott and Rogers*, 1990) over the relatively long
923 expansion periods in the confined vessel and internal turbulence during the expansion leading
924 to heterogeneously supersaturated water vapor and temperature fields. These artifacts can bias
925 IN measurements.

926 CFDCs are the most widely used technique to measure INPs in the atmosphere, but
927 their inability to quantify INPs at high temperatures is an issue that exists due to the physical
928 principals of operation, the limited sample volume (typically 1 to 2 L min⁻¹) and background
929 frost formation in the chamber over periods of operation. Based on the operational equations
930 in *Rogers* (1988), the warmest operating temperature of a CFDC is approximately -6.5 °C ,
931 controlled by the fact that the warmest wall cannot exceed 0 °C . Low sample volumes
932 necessitate integration over longer sample periods and result in a general lower detection limit
933 of 0.2 L^{-1} of sampled air, absent any particle pre-concentration (*Prenni et al.*, 2009).
934 According to *Tobo et al.* (2013), the highest temperature that can be achieved in a CFDC is -9
935 °C . Above this threshold, temperature and ice saturation conditions cannot be maintained in
936 the chamber. *Rogers et al.* (2001) and other papers since have identified measurement issues
937 due to frost emanating from the walls of the chamber when the dew point temperature of the
938 sample air is not effectively controlled, although this appears to be an operational issue that

939 can be mitigated if monitored properly, and will be most obtrusive for atmospheric sampling
940 scenarios.

941

942 **4.3. Stochastic nature of freezing and time dependence**

943

944 The longstanding discussion of the stochastic theory (i.e., the freezing process is time-
945 dependent) vs. the deterministic approximation (i.e., freezing occurs at specific temperature
946 and humidity conditions) of heterogeneous freezing has introduced another complication
947 towards complete understanding of heterogeneous ice nucleation in the atmosphere (*Vali*,
948 2014). Many studies have attempted to characterize ice nucleation based on the classical
949 nucleation theory (CNT), which incorporates a nucleation rate (*Murray et al.*, 2012;
950 *Kashchiev*, 2000; *Mullin*, 2001). In this treatment, the ice nucleation process is always of a
951 stochastic nature (i.e., time-dependent; *Bigg*, 1953; *Vali*, 1994; *Vali*, 2014). According to the
952 nucleation rate approach, the heterogeneous ice nucleation rate is strongly sensitive to INP
953 size and the kinetic activation energy of the ice embryo on the nucleating site/surface at a
954 specific temperature (*Khvorostyanov and Curry*, 2000; *Fletcher*, 1962). A few variants of the
955 CNT-based approaches have been developed over the past few decades. These approaches
956 assume uniform surface characteristics and only one ice nucleation probability (i.e., a single
957 contact angle), nominally categorized as the single component nucleation rate approach (e.g.,
958 *Bigg*, 1953). Several recent studies have applied a probability density function (PDF) of
959 contact angles and active sites over the INP surface in CNT, or in other words described a
960 distribution of nucleation efficiencies, bridging the gap between the stochastic theory and the
961 deterministic treatment (*Marcolli et al.*, 2007; *Lüönd et al.*, 2010; *Kulkarni et al.*, 2012;
962 *Niedemeier et al.*, 2011; *Wright and Petters.*, 2013; *Broadley et al.*, 2012).

963 The deterministic or time-independent singular approximation has been developed as
964 an alternative option to quantitatively understand atmospheric ice nucleation. The concept was
965 first developed by *Levine* (1950), while the term “active sites” per surface area was introduced
966 by *Fletcher* (1969). More recently, *Connolly et al.* (2009) introduced the n_s density
967 parameterization (see Sect. 2.4). This specific approach neglects the time dependence of
968 freezing, and assumes that a characteristic condition (e.g., temperature) must be met to
969 nucleate ice. The semi-deterministic forms of the singular approach have a cooling rate
970 dependence incorporated (*Vali*, 2008; *Herbert et al.*, 2014). Predicting ice nucleation from a
971 singular perspective does not require a vast knowledge of particle-specific parameters (e.g.,
972 surface composition, structures, surface tension and solubility) that are particular to each ice

973 nucleus and, therefore, enables ice nucleation parameterization to be relatively simple and
974 efficient compared to the CNT-based approaches (*Murray et al.*, 2011).

975 The assumption that the time dependence of the freezing of droplets is of secondary
976 importance when compared to temperature dependence is supported by a recent modeling
977 sensitivity study that shows that common INPs are substantially more sensitive to temperature
978 than to time (*Ervens and Feingold*, 2013). Furthermore, while *Broadley et al.* (2012) shows
979 that freezing by illite NX is time-dependent through isothermal experiments, the shift in
980 freezing temperature on changing cooling rates by an order of magnitude is less than 0.6 °C,
981 which is within the experimental uncertainty. A similar observation of weak time dependence
982 of immersion freezing for various types of suspended samples, inferred by comparing the
983 results with varied cooling rates from 0.01 °C min⁻¹ to 1 °C min⁻¹, is reported by *Wright et al.*
984 (2013).

985 In the context of dry-dispersed measurements, the sensitivity of the ice nucleation to a
986 possible time dependence, and the respective influence on n_s , was examined to further discern
987 its importance and uncertainty. Specifically, a contact angle distribution was fitted to the
988 LACIS measurements and was used, together with the soccer ball model (SBM; *Niedermeier*
989 *et al.*, 2011 and 2014), to simulate frozen fractions for different residence times varying over
990 four orders of magnitude (i.e., 1, 10, 100 and 1000 s residence time). These frozen fractions
991 were then used to calculate n_s , shown as lines in Fig. 9. More specifically, frozen fractions for
992 500 nm diameter illite NX particles were calculated based on SBM to obtain $n_s(T)$ spectra. To
993 accomplish this, a contact angle distribution was used which was derived based on LACIS
994 data for the illite NX particles as shown in this work, resulting in values of 1.90 rad for the
995 mean and 0.27 rad for the width of the contact angle distribution. Frozen fractions were
996 obtained for ice nucleation residence times of 1, 10, 100 and 1000 s. An increase in the
997 residence time by a factor of 10 resulted in a shift of approximately 1 °C towards higher
998 freezing temperatures. This is similar to the results found in a previous study by *Welti et al.*
999 (2012) for measurements of kaolinite rich clay minerals. Indeed, $n_{s,geo}$ data obtained from
1000 AIDA agree within the measurement uncertainty with LACIS data without accounting for
1001 time dependence. These results suggest that time dependence of immersion freezing for illite
1002 NX particles can be neglected as a factor in the comparisons shown in Figs. 4, 5 and 6. They
1003 also imply that the immersion freezing nature of illite NX is only slightly dependent on
1004 cooling rate across a wider range of temperatures (as compared to a -26 °C to -37 °C range as
1005 shown in *Broadley et al.*, 2012), regardless of the sample preparation process.

1006

1007 **4.4. Potential effect of agglomerates**

1008

1009 As seen in the particle surface area distributions (Fig. 2) and agglomerated-fractions
1010 based on a relative comparison to D_{95} , aggregates are rather persistent and dominant for most
1011 of the dry-dispersed particle measurements. Since dry aggregates can have large
1012 ‘supermicron’ sizes, they may have different IN propensities and efficiencies (*Wheeler et al.*,
1013 2014) as compared to the smaller sizes investigated in the present study (i.e., up to 1000 nm
1014 from PINC). Further, the degree of agglomeration may conceivably affect the surface area
1015 exposed to liquid water when suspended in supercooled droplets. Hence, an overall
1016 quantification of the effect of agglomerates is difficult. Moreover, the degree of
1017 agglomeration seems to vary from experiment to experiment, introducing diversity on the
1018 estimation of S_{total} of particles and n_s for dry-dispersed particle measurements. For instance, a
1019 combination of several methods for particle dispersion and subsequent particle size selection
1020 was employed for particle generation from illite NX samples. Further, most of the dry
1021 dispersion techniques used upstream impactors to filter out large agglomerated particles and
1022 avoid counting these large particles as INPs. The different types of dispersion methods,
1023 impactors and size segregating instruments used in the present work are listed in the
1024 Supplement Table S1. These different aerosol generation processes may have caused different
1025 degrees of agglomeration. This may in part explain why n_s measurements obtained using dry
1026 dispersion techniques deviated from those using suspension measurements. Further
1027 quantification of the influences of different methods for particle dispersion, size-segregation
1028 and particle impaction/filtration on the estimation of S_{total} and n_s is an important topic for
1029 future works.

1030 In contrast, in suspension experiments, illite NX samples were directly suspended in
1031 water. Despite no pre-treatments (e.g., pre-impaction or size segregation), suspended particles
1032 appeared adequately de-agglomerated (Fig. 2a). Though the number of immersed particles can
1033 vary from droplet to droplet and the random placement of particles in the drop may have an
1034 effect on the n_s values, the n_s spectra from suspension measurements are in reasonable
1035 agreement with slight deviations even over a wide range of wt% of illite NX samples (the
1036 Supplement Figs. 6, 8, S4-S8). Thus, the influence of the random placement of particles in the
1037 drop and agglomeration on the n_s estimation for suspension measurements seems small. To
1038 support this, *Wright and Petters (2013)* and *Hader et al. (2014)* simulated the role of a
1039 statistical distribution in drops. The authors demonstrated that the random component due to
1040 drop placement seemed to be small relative to the statistical variation due to nucleation

1041 probability. Hence, assuming the degree of agglomeration or flocculation is similar in all
1042 suspension samples, the degree of agglomeration and the random placement of particles in the
1043 drop may lead to less pronounced deviations in n_s when compared to dry-dispersed
1044 measurements.

1045

1046 **4.5. Nucleation mode dependence**

1047

1048 While all suspension methods only measured immersion mode freezing of the illite
1049 NX particles, a contribution of other nucleation or freezing modes cannot be ruled out for dry-
1050 dispersed particle measurements. Hence, we now discuss inferences in the present
1051 experiments regarding the mode dependency of the ice nucleation ability of illite NX
1052 particles. Figure 10a and b show the comparison of n_s derived from the two different
1053 operation types of FRIDGE measurements. For instance, ‘default mode’ considers deposition
1054 mode nucleation and immersion mode freezing of dry particles in which RH_w is scanned
1055 upwards and ‘imm.mode’ counts immersion freezing of suspended particles in which the
1056 particles are first washed into droplets and then placed on the substrate. With these two
1057 different operational modes, FRIDGE investigated the ice nucleation ability of both dry and
1058 droplet suspended particles deposited on a substrate (see the Supplementary Methods).
1059 FRIDGE scans RH_{ice} and RH_w (low to high) at a constant temperature. During such scans an
1060 abrupt increase in an activated ice fraction near water saturation as well as the highest N_{ice} is
1061 typically observed. We consider ice crystals formed at the highest RH_w (near 100% RH_w) as a
1062 measure of immersion N_{ice} from dry-dispersed particle measurements in this study. Some
1063 default runs of FRIDGE show much higher $n_{s,BET}$ values compared to the immersion mode
1064 runs. This difference may be a consequence of the different IN efficiencies of nucleation
1065 modes (deposition + immersion vs. immersion alone) in the examined temperature range (-25
1066 $^{\circ}C < T < -18$ $^{\circ}C$), the different sample preparation processes (dry or suspended sample),
1067 effects of agglomeration or a combination of the three. We note that a major difference
1068 between the two measurement setups is the pressure within the instrument. For instance,
1069 default conditions involve processing at a few hPa of water vapor while the immersion
1070 measurements are conducted at atmospheric pressure. In addition, corrective post-analysis of
1071 droplet/ice separation was taken into account in this study, so that errors from counting large
1072 droplets as ice crystals were successfully removed. Interestingly, our comparison suggests that
1073 n_s values derived from the FRIDGE default mode seem similar to those from MRI-DCECC, in
1074 which experiments were carried out with a high degree of particle agglomeration (Fig. 2c).

1075 Some other variations on applied methods suggest nucleation mode effects on the IN
1076 efficiency of illite NX particles at lower temperatures (Fig. 10c and d). For instance, the
1077 comparison between ZINC and IMCA-ZINC show about an order of magnitude diversity in
1078 $n_{s,BET}$ beyond experimental uncertainties at -33 °C, suggesting a mode-dependent IN
1079 efficiency of clay minerals at this temperature. This observation is consistent with a statement
1080 that the immersion freezing parameterization from CNT may not reliably predict the activated
1081 fraction observed at $RH_w > 100\%$ as observed from condensation freezing (*Welti et al.*, 2014).
1082 However, this is in contrast to observations indicated by PNNL-CIC below -25 °C and to
1083 results presented in *Wex et al.* (2014), where $n_{s,geo}$ obtained from kaolinite measurements
1084 made with LACIS and the CSU-CFDC (at $104\% > RH_w > 106\%$ for the latter) agreed well.
1085 When a freezing point depression is taken into account, even data obtained with the CSU-
1086 CFDC for water-vapor-sub-saturated conditions is in agreement with data obtained from both
1087 LACIS and CSU-CFDC at water-vapor super-saturated conditions. Concerning data presented
1088 here, PNNL-CIC and IMCA-ZINC measure condensation/immersion and purely immersion
1089 mode freezing efficiency of particles, respectively, and are in reasonable agreement within
1090 experimental uncertainties (Fig. 10c and d). Thus, the observed inconsistencies between
1091 methods should be subject to further methodological improvements to provide accurate data
1092 as a basis for model parameterization. Similar heterogeneous ice nucleation mode-dependent
1093 observations were made by our EDB experiments. We observed that n_s values derived from
1094 contact freezing experiments were higher than those derived from immersion experiments
1095 (Fig. 10c and d). As described in the Supplementary Methods, immersion mode experiments
1096 were performed for the droplets, which were not activated via contact freezing.

1097

1098 **4.6. Effect of mineralogical properties: which component of illite NX nucleates ice?**

1099

1100 *Atkinson et al.* (2013) suggested that the mass fraction of K-feldspar in a sample can
1101 be used as a scaling factor to estimate the n_s values of other K-feldspar containing dust and
1102 soil samples. *O'Sullivan et al.* (2014) showed that this scaling rule could be used as an
1103 approximate predictor for the n_s of soil samples once the biological ice-nucleating particles
1104 were deactivated. However, inspection of Fig. 6 reveals that the line based on 14% feldspar
1105 (assuming all microcline) significantly over predicts the n_s values for illite NX. There are a
1106 number of reasons why this might be.

1107 The K-feldspar sample used by *Atkinson et al.* (2013) was the British Chemical
1108 Standard Chemical Reference Material (BCS-CRM) number 376/1 and X-ray diffraction

1109 analysis shows that the crystal structure is consistent with that of microcline. Microcline is
1110 one possible form of a K-feldspar and, as discussed above, other feldspars are sanidine and
1111 orthoclase, which have distinct crystal structures. The ice nucleation abilities of sanidine and
1112 orthoclase are not yet published, but given they have different crystal structures they may
1113 have different nucleating abilities. Unfortunately, the X-ray diffraction analysis of illite NX is
1114 unable to identify the K-feldspar(s) present in illite NX, although the mineralogical analysis
1115 conducted as part of this study concluded that there was no detectable microcline in illite NX.
1116 Hence, one explanation for the K-feldspar scaling rule not working for illite NX is that there is
1117 only a trace of the strongly ice active microcline present in illite NX. For suspension
1118 measurements, only the 0.0014% microcline parameterization reproduces the slope and
1119 magnitude of the illite NX data in Fig. 6, but this quantity of microcline is well below the
1120 detection limit of the X-ray diffraction technique. Perhaps, in the case of illite NX, it may not
1121 be the feldspar which triggers nucleation, but instead it could be another mineral present in
1122 this sample. For example, *Atkinson et al.* (2013) found that a quartz sample nucleated ice
1123 more efficiently than the clay minerals, but less efficiently than the feldspar samples they
1124 used. At about -28 °C, they reported an n_s of $\sim 10^{10} \text{ m}^{-2}$. The X-ray analysis in this study
1125 revealed the presence of 3% quartz, hence we would predict an n_s of $3 \times 10^8 \text{ m}^{-2}$, which is
1126 consistent with the illite NX data. Finally, an alternative explanation is that the surfaces of K-
1127 feldspars are chemically altered in illite NX. The surfaces of feldspars are known to transform
1128 to an amorphous silicate which can then recrystallize as a clay if exposed to an acidic
1129 environment. *Wex et al.* (2014) suggested that it was the acid processing of K-feldspar which
1130 deactivated Fluka-kaolinite. It is feasible that the surfaces of feldspar grains in illite NX have
1131 at some point become deactivated. More quantitative investigations of the acid processing of
1132 both reference and atmospherically relevant materials and its influence on their immersion
1133 mode ice nucleation efficiencies are needed.

1134 Recently, re-partitioning of soluble components of both swelling and non-swelling
1135 clay minerals and their effect on cloud condensation nucleation activity was reported (*Sullivan*
1136 *et al.*, 2010; *Kumar et al.*, 2011; *Garimella et al.*, 2014). To address a potential importance of
1137 this effect on the ice-nucleating activity of illite NX in the wet dispersion experiments, we
1138 have measured the concentration of cations released by the illite NX sample placed into
1139 deionized water as a function of time, as described in Sect. 3.1 (i.e., Fig. 3).

1140 It is instructive to compare the quantity of cations released by illite NX into an
1141 aqueous environment with the value of the Cation Exchange Capacity (CEC) for illite, which
1142 is known to be 25 to 40 cmol kg^{-1} (*Meunier and Velde*, 2004). CEC is defined as the amount of

1143 cations retained by all the negative charges in 100g of clay immersed in water at pH 7 (e.g.,
1144 see *Meunier*, 2005). Per this definition, CEC describes the total quantity of exchangeable
1145 cations, including interlayer cations which are in fact not accessible for substitution in non-
1146 swelling clays. The molar fraction of external cations, located on the basal planes of the
1147 crystals and on the crystal edges is roughly evaluated for illites as 20% of the total CEC,
1148 yielding 5 to 8 cmol kg⁻¹ (*Wilson*, 2013). Remarkably, the total amount of all cations (K⁺,
1149 Mg²⁺ and Ca²⁺) released within the first hour by illite NX, if recalculated with account for
1150 cation valence and for the actual mass of illite in the aqueous suspension (0.1 g), gives the
1151 number 7.5 cmol kg⁻¹, which corresponds nicely with the upper bound of the external CEC (8
1152 cmol kg⁻¹). Furthermore, *Grim* (1953) has shown that the CEC of illite increases with
1153 decreasing size of the clay particle size, with the upper bound (~40 cmol kg⁻¹) being
1154 characteristic for illite with a particle size below 100 nm. This is again consistent with the
1155 very small size of particles in illite NX.

1156 These findings have two potential implications for the measurements of illite NX ice-
1157 nucleating efficiency obtained with different instruments. First, in the methods where dry illite
1158 NX particles are activated to droplets prior to cooling, the concentration of cations released
1159 into the water surrounding the particles is still far from the equilibrium and is a function of the
1160 residence time (e.g., ~2-3 s for LACIS, ~4 s for PINC, ~12 s for PNNL-CIC, and over the
1161 range of several tens of seconds to a few minutes for AIDA depending on initial chamber T
1162 and RH). At the same time, the amount of external cations retained on the surface of illite
1163 particles determines the charge properties, such as charge distribution landscape and zero
1164 charge point. A potential importance of the surface charge of hematite particles for their IN
1165 activity was suggested recently in *Hiranuma et al.* (2014b). These considerations, however
1166 speculative, might shed some light on the observed scattering of experimentally measured
1167 values of n_s . Second, for the freezing measurements where the illite rich sample was
1168 suspended in water prior to cooling, all accessible external cations were already released into
1169 the aqueous environment. In these cases the concentration of cations in the droplets is a
1170 function of mass concentration of illite in suspension. To access high freezing temperatures,
1171 high concentrations of illite are needed in the droplet assay techniques, resulting in the
1172 possibility that not all cations are released into solution due to the inhibition of the ion
1173 exchange process. Again, this would change the surface charge distribution and potentially
1174 affect the ice-nucleating efficiency of illite particles. If wet particle generation (dispersion of
1175 aqueous suspension by means of a pressurized air atomizer) is used, the redistribution of
1176 cations between suspended particles may be an issue, as suggested by *Garimella et al.* (2014)

1177 for the case of CCN experiments. Further studies of samples without modification or ageing
1178 after dry dispersion or wet suspension are needed to get a better idea of the method inter-
1179 comparison.

1180 5. Conclusion

1181

1182 The framework of the present work is designed to advance the existing state of
1183 knowledge regarding IN measurement techniques. After ICIS-2007, there has been an
1184 increase in new instrument development, especially off-line, substrate-supported cold stage
1185 techniques, and modifications of existing online techniques. Concepts to formulate area-
1186 scaled IN efficiency with n_s parameters have also since been introduced to the community.
1187 These improvements are comprehensively evaluated in this work.

1188 The partners of the INUIT group and external partners have for the first time identified
1189 and shared a reference mineral dust sample (illite NX) in order to obtain a comprehensive
1190 dataset for evaluating immersion freezing properties of atmospherically relevant particles
1191 across a wide range of particle concentrations, temperatures, cooling rates and nucleation
1192 times. Illite NX samples were extensively characterized for their physico-chemical properties
1193 before they were distributed to INUIT partners and collaborators. Both bulk and single
1194 particle elemental composition analyses were conducted by XRD and EDX analyses,
1195 respectively.

1196 A total of seventeen IN measurement techniques were inter-compared based on their
1197 immersion freezing measurements. Our inter-comparison exercise provided unique results that
1198 would not have been achieved by individual investigators in isolation. Both consistencies and
1199 discrepancies among the instruments have been identified. Our results suggest that the immersion
1200 freezing efficiency (i.e., n_s) of illite rich clay minerals is relatively independent of droplet size,
1201 mass percent of illite NX sample in droplets for the methods examining suspensions, physical
1202 size of illite NX particles for the methods examining dry-dispersed particles and cooling rate
1203 during freezing within typical experimental uncertainties, verifying the premise of the n_s
1204 concept (i.e., size independency for submicron illite NX particles, strong temperature
1205 dependency and weak time dependency of immersion freezing for illite rich clay mineral
1206 particles).

1207 Furthermore, comparisons of the suspension subsets against the dry-dispersed particle
1208 techniques were performed. Dry samples alone showed higher n_s values compared to the pre-
1209 suspended samples above -27 °C. A possible explanation for this deviation (i.e., n_s from dry-
1210 dispersed methods $> n_s$ from suspension methods) may be the surface modification of the illite
1211 NX particles (e.g., due to ion dissolution effects in the aqueous suspension).

1212 Comparisons of the absolute values of $\Delta\log(n_s)/\Delta T$ as an ice activation parameter
1213 suggest that the predominant freezing sites of illite NX particles exist in a temperature range
1214 between $-20\text{ }^\circ\text{C}$ and $-27\text{ }^\circ\text{C}$ for suspension experiments. In comparison to previous
1215 measurements, our synergetic work, which covers a wide temperature range, shows a similar
1216 result to the Broadley parameterization (B12), and our overall fit for the low temperature
1217 region below $-27\text{ }^\circ\text{C}$ also agrees with the Niemand parameterization (N12).

1218 Overall accuracy and precision of the IN measurement techniques was examined by
1219 evaluating T -binned (i.e., $1\text{ }^\circ\text{C}$ bins) $n_s(T)$ data derived from all seventeen instruments for the
1220 temperature range from $-11\text{ }^\circ\text{C}$ to $-37\text{ }^\circ\text{C}$. Our analysis revealed that discrepancies among
1221 measurements were within about $8\text{ }^\circ\text{C}$ in terms of temperature and up to three orders of
1222 magnitude with respect to n_s . This diversity is much larger than the individual uncertainties of
1223 each instrument, suggesting that all instruments may be reasonably precise but it is still
1224 difficult to find overall accuracy of current IN measurement techniques, at least while using
1225 illite NX as the standard and allowing partners to investigate it independently. In addition, two
1226 different n_s metrics, $n_{s,\text{geo}}$ and $n_{s,\text{BET}}$, were compared, and we found that $n_{s,\text{BET}}$ is a better proxy
1227 for suspension-based IN measurements, while $n_{s,\text{geo}}$ is better for dry-dispersed particle
1228 measurements.

1229 Other than the inter-comparison aspects described above, several important
1230 implications were inferred from our study and enhanced our basic knowledge of immersion
1231 freezing. First, the existence of only a comparably small contribution of time dependence to
1232 the inter-comparison was reconciled by the SBM simulation. Specifically, a change of the
1233 residence time, from 1 to 10 s, shifts n_s values towards higher temperatures by only about 1
1234 $^\circ\text{C}$. Second, several nucleation modes and their contribution to nucleation efficiency were also
1235 evaluated. A comparison among EDB, ZINC and IMCA-ZINC below $-25\text{ }^\circ\text{C}$ implied some
1236 mode dependencies. Likewise, a mode dependency was also pronounced based on FRIDGE
1237 results at temperatures above $-25\text{ }^\circ\text{C}$. Third, immersion freezing experiments were performed
1238 with both polydisperse and size-selected illite NX particles for the AIDA-CECC, MRI-
1239 DCECC and CSU-IS measurements, and size independence of n_s for immersion freezing of
1240 submicron illite NX particles (DMA size-selected 200, 300 and 500 nm diameter) was also
1241 demonstrated. Finally, our observations show that temperature is the major variable
1242 influencing the immersion freezing of illite NX particles, as the n_s values in general increase
1243 while temperature decreases. In addition, our results of n_s and absolute values of $\Delta\log(n_s)/\Delta T$
1244 distributions across a wide range of temperatures imply that clay minerals may contain
1245 various freezing activation energies, and the immersion freezing nature of clay minerals (e.g.,

1246 illite NX) in a wide range of temperatures cannot be fitted by simple exponential functions but
1247 are governed by a hybrid of multi-exponential functions (a combination of scaled A13 and
1248 N12 parameterizations).

1249 Though we shared identical test samples with each other, it is still difficult to compare
1250 n_s results because sample preparation techniques and measurement methods (e.g., particle
1251 dispersion and size distribution characterization) differ from group to group, which can result
1252 in different degrees of agglomeration or different nucleation modes. Therefore, a continued
1253 investigation to obtain further insights into consistencies or diversity of IN measurement
1254 techniques from an experimental perspective is important to explore freezing conditions for
1255 specific compositions and more atmospherically relevant particles (e.g., soil dusts and long
1256 range transported weathered dusts). In parallel, an empirically constrained model including
1257 parameterizations of immersion freezing that correctly and efficiently represent particle-
1258 specific experimental data is also in high demand for overall predictions of current and future
1259 climate. We demonstrated that the n_s formulation offers a simplified expression for
1260 quantitatively parameterizing immersion freezing. Further developments of more simplified
1261 (efficient but accurate) descriptions, constrained by more accurate IN counting techniques, of
1262 governing atmospheric IN processes are needed.

1263 **Acknowledgements**

1264

1265 Part of this work is funded by Deutsche Forschungsgemeinschaft (DFG) under
1266 contracts BU 1432/4-1, DI 1539/1-1, KO2944/2-1, MO668/4-1 and WE 4722/1-1 within
1267 Research Unit FOR 1525 (INUIT). The authors acknowledge partial financial support by
1268 Deutsche Forschungsgemeinschaft and Open Access Publishing Fund of Karlsruhe Institute of
1269 Technology. The authors gratefully acknowledge skillful and continuous support from their
1270 technical teams. G. Kulkarni acknowledges support from the Department of Energy (DOE)
1271 Atmospheric System Research Program and thanks J. Fast for useful discussion. Battelle
1272 Memorial Institute operates the Pacific Northwest National Laboratory for DOE under
1273 contract DE-AC05-76RLO 1830. Z. A. Kanji acknowledges funding from Swiss National
1274 Funds. P. J. DeMott and T. Hill were funded by NSF grant award number AGS-1358495. M.
1275 A. Tolbert and G. P. Schill were funded by NSF Grant AGS 1048536. The MRI-DCECC
1276 work was partly funded by JSPS KAKENHI Grant Numbers 23244095. T. P. Wright, J. D.
1277 Hader, and M. D. Petters were funded by NSF Grant AGS 1010851. B. J. Murray, D.
1278 O'Sullivan and T. F. Whale acknowledge the Natural Environment Research Council
1279 (NE/K004417/1; NE/I020059/1; NE/I013466/1; NE/I019057/1) and The European Research
1280 Council (240449 – ICE) for funding. D. Niedermeier acknowledges financial support from the
1281 Alexander von Humboldt-foundation, Germany.

1282 T. C. J. Hill would like to thank E. Levin and C. McCluskey for generation of size-
1283 selected particles. K. Diehl would like to thank S. K. Mitra for technical support on M-AL and
1284 M-WT and fruitful discussions. A. Kiselev and A. Peckhaus acknowledge O. Dombrowski for
1285 her support in IC measurements. N. Hiranuma thanks C. Anquetil-Deck for useful discussion.
1286 N. Hiranuma and G. Kulkarni thank T. Kisely and R. Ahmad for the N₂ BET and H₂O BET
1287 measurements, respectively. M. Ebert acknowledges R. Petschik for the additional high
1288 precision XRD measurements. N. Hiranuma and O. Möhler gratefully acknowledge technical
1289 support from M. Koyro and F. Schwartz for setting up the database for storing and updating
1290 the INUIT laboratory results. N. Hiranuma also thanks the AIDA technical team, including R.
1291 Buschbacher, T. Chudy, O. Dombrowski, E. Kranz, G. Scheurig and S. Vogt, for their
1292 professional support for the chamber maintenance and operation.

1293 **Author contributions**

1294

1295 J. Curtius and O. Möhler proposed the framework of this collaborative multi-
1296 institutional laboratory work. The overall manuscript, coordinated and led by N. Hiranuma,
1297 was a collaborative effort of the partners of the INUIT group and external partners. C. Budke
1298 and T. Koop designed and conducted the BINARY experiments, analyzed the data, and
1299 contributed the BINARY text. T. C. J. Hill carried out the CSU-IS measurements, analyzed
1300 the data, and contributed to the CSU-IS text. B. J. Murray, D. O’Sullivan and T. F. Whale
1301 performed the Leeds-NIPI experiments, analyzed the data, and contributed to the Leeds-NIPI
1302 text. K. Diehl performed the experiments and data analysis of M-AL and W-WT, and K. Diehl
1303 also contributed to their method summary text. J. D. Hader performed the NC State-CS
1304 experiments and analyzed the data, T. P. Wright contributed the analysis software, M. D.
1305 Petters designed the experiments, and J. D. Hader and M. D. Petters contributed to the NC
1306 State-CS text. G. P. Schill and M. A. Tolbert conducted the CU-RMCS experiments, analyzed
1307 the data, and contributed to the CU-RMCS text. N. Hiranuma and O. Möhler conceived the
1308 AIDA experiments, analyzed and discussed the results and contributed to the AIDA text. P. J.
1309 DeMott, E. J. T. Levin and C. S. McCluskey performed CSU-CFDC experiments, analyzed
1310 the data, and contributed to the CSU-CFDC text. N. Hoffmann and A. Kiselev carried out the
1311 EDB measurements with input on experimental techniques from T. Leisner and SEM
1312 measurements and contributed to the associated data analysis and text. Björn Nillius and
1313 Fabian Frank performed the FINCH experiments and analyzed the data, and D. Rose
1314 contributed to the FINCH uncertainty analysis and method summary text. A. Danielczok and
1315 H. Bingemer conducted the FRIDGE experiments, analyzed the data, and contributed to the
1316 FRIDGE text. S. Augustin-Bauditz did the LACIS experiments, D. Niedermeier derived
1317 contact angle distributions with SBM, and H. Wex performed SBM calculations and
1318 contributed to the LACIS text. M. Murakami, K. Yamashita, T. Tajiri and A. Saito designed
1319 and performed the MRI-DCECC experiments with assistance and contributions from N.
1320 Hiranuma and O. Möhler, K. Yamashita and N. Hiranuma analyzed the MRI-DCECC data,
1321 and K. Yamashita contributed to the method summary text. Z.A. Kanji conducted the PINC
1322 experiments, Y. Boose analyzed the data, Y. Boose and Z.A. Kanji interpreted and discussed
1323 the PINC data, and contributed to the PINC text. G. Kulkarni carried out the PNNL-CIC
1324 measurements, analyzed the data, and contributed to the PNNL-CIC text. A. Welti performed
1325 the IMCA-ZINC experiments, analyzed the data, and A. Welti and Z. A. Kanji contributed to

1326 the supplementary text. XRD measurements and analysis of illite NX were conducted by M.
1327 Ebert, K. Kandler and S. Weinbruch, and M. Ebert contributed the XRD text. IC
1328 measurements and analysis were carried out by A. Peckhaus and A. Kiselev, and A. Kiselev
1329 contributed to the IC text. DLS measurements and analysis were performed by K.
1330 Dreischmeier, and K. Dreischmeier also contributed to the DLS text. N. Hiranuma interpreted
1331 and analyzed the compiled data and wrote the paper. A. Kiselev and B. J. Murray co-wrote
1332 Sect. 4.6 with N. Hiranuma. All authors discussed the results and contributed to the final
1333 version of the manuscript.

1334 **References**

1335

1336 Ardon-Dryer, K., Levin, Z., and Lawson, R. P.: Characteristics of immersion freezing nuclei
1337 at the South Pole station in Antarctica, *Atmos. Chem. Phys.*, 11, 4015–4024, doi:10.5194/acp-
1338 11-4015-2011, 2011.

1339

1340 Atkinson, J. D., Murray, B. J., Woodhouse, M. T., Carslaw, K., Whale, T. F., Baustian, K.,
1341 Dobbie, S., O’Sullivan, D., and Malkin, T. L.: *Nature*, 498, 355–358,
1342 doi:10.1038/nature12278, 2013.

1343

1344 Augustin-Bauditz, S., Wex, H., Kanter, S., Ebert, M., Stolz, F., Prager, A., Niedermeier, D.
1345 and Stratmann, F.: The immersion mode ice nucleation behavior of mineral dusts: A
1346 comparison of different pure and surface modified dusts, *Geophys. Res. Lett.*, 41, 7375–7382,
1347 doi:10.1002/2014GL061317, 2014.

1348

1349 Bickmore, B. R., Nagy, K. L., Sandlin, P. and Crater, T. S.: Quantifying surface areas of clays
1350 by atomic force microscopy, *American Mineralogist*, 87, 780–783, 2002.

1351

1352 Bigg, E. K.: The supercooling of water, *Proc. Phys. Soc. B*, 66, 688–694, doi:10.1088/0370-
1353 1301/66/8/309, 1953.

1354

1355 Bigg, E. K., A new technique for counting ice-forming nuclei in aerosols. *Tellus*, 9: 394–400.
1356 doi:10.1111/j.2153-3490.1957.tb01895.x, 1957.

1357

1358 Bingemer, H., Klein, H., Ebert, M., Haunold, W., Bundke, U., Herrmann, T., Kandler, K.,
1359 Müller-Ebert, D., Weinbruch, S., Judt, A., Wéber, A., Nillius, B., Ardon-Dryer, K., Levin, Z.,
1360 and Curtius, J.: Atmospheric ice nuclei in the Eyjafjallajökull volcanic ash plume, *Atmos.*
1361 *Chem. Phys.*, 12, 857–867, doi:10.5194/acp-12-857-2012, 2012.

1362

1363 Boucher, O., Randall, D., Artaxo, P., Bretherton, C., Feingold, G., Forster, P., Kerminen, V.-
1364 M., Kondo, Y., Liao, H., Lohmann, U., Rasch, P., Satheesh, S. K., Sherwood, S., Stevens, B.,
1365 and Zhang, X. Y.: Clouds and Aerosols. In: *Climate Change 2013: The Physical Science*
1366 *Basis. Contribution of Working Group I to the Fifth Assessment Report of the*
1367 *Intergovernmental Panel on Climate Change* [Stocker, T. F., D. Qin, G.-K. Plattner, M.
1368 Tignor, S. K. Allen, J. Boschung, A. Nauels, Y. Xia, V. Bex and P. M. Midgley (eds.)].
1369 Cambridge University Press, Cambridge, United Kingdom and New York, NY, USA, 571–
1370 657, 2013.

1371

1372 Broadley, S. L., Murray, B. J., Herbert, R. J., Atkinson, J. D., Dobbie, S., Malkin, T. L.,
1373 Condliffe, E., and Neve, L.: Immersion mode heterogeneous ice nucleation by an illite rich
1374 powder representative of atmospheric mineral dust, *Atmos. Chem. Phys.*, 12, 287–307,
1375 doi:10.5194/acp-12-287-2012, 2012.

1376

1377 Brunauer, S., Emmett, P. H., and Teller, E.: Adsorption of gases in multimolecular layers, *J.*
1378 *Am. Chem. Soc.*, 60, 309–319, doi:10.1021/ja01269a023, 1938.

1379

1380 Budke, C. and Koop, T.: BINARY: an optical freezing array for assessing temperature and
1381 time dependence of heterogeneous ice nucleation, *Atmos. Meas. Tech. Discuss.*, 7, 9137–
1382 9172, doi:10.5194/amtd-7-9137-2014, 2014.

1383

1384 Bundke, U., Nillius, B., Jaenicke, R., Wetter, T., Klein, H., and Bingemer, H.: The fast ice
1385 nucleus chamber FINCH, *Atmos. Res.*, 90, 180–186, doi:10.1016/j.atmosres.2008.02.008,
1386 2008.

1387

1388 Chou, C., Stetzer, O., Weingartner, E., Jurányi, Z., Kanji, Z. A., and Lohmann, U.: Ice nuclei
1389 properties within a Saharan dust event at the Jungfraujoch in the Swiss Alps, *Atmos. Chem.*
1390 *Phys.*, 11, 4725–4738, doi:10.5194/acp-11-4725-2011, 2011.

1391

1392 Christenson, H.: Two-step crystal nucleation via capillary condensation, *Cryst. Eng. Comm.*,
1393 15, 2030–2039, doi:10.1039/C3CE26887J, 2013.

1394

1395 Connolly, P. J., Möhler, O., Field, P. R., Saathoff, H., Burgess, R., Choulaton, T., and
1396 Gallagher, M.: Studies of heterogeneous freezing by three different desert dust samples,
1397 *Atmos. Chem. Phys.*, 9, 2805–2824, doi:10.5194/acp-9-2805-2009, 2009.

1398

1399 Cwilong, B. M.: Sublimation centers in a Wilson chamber, *Proc. Roy. Soc. A*, 190, 137–143,
1400 doi:10.1098/rspa.1947.0066, 1947.

1401

1402 DeMott, P. J. and Rogers, D. C.: Freezing nucleation rates of dilute solution droplets
1403 measured between -30° and -40 °C in laboratory simulations of natural clouds. *J. Atmos. Sci.*,
1404 47, 1056–1064, doi:http://dx.doi.org/10.1175/1520-
1405 0469(1990)047<1056:FNRODS>2.0.CO;2, 1990.

1406

1407 DeMott, P. J.: Quantitative descriptions of ice formation mechanisms of silver iodide-type
1408 aerosols, *Atmos. Res.*, 38, 63–99, doi:10.1016/0169-8095(94)00088-U, 1995.

1409

1410 DeMott, P. J. and Coauthors: Resurgence in ice nuclei measurement research, *B. Am.*
1411 *Meteorol. Soc.*, 92, 1623–1635, doi:http://dx.doi.org/10.1175/2011BAMS3119.1, 2011.

1412

1413 DeMott, P. J., Prenni, A. J., McMeeking, G. R., Sullivan, R. C., Petters, M. D., Tobo, Y.,
1414 Niemand, M., Möhler, O., Snider, J. R., Wang, Z., and Kreidenweis, S. M.: Integrating
1415 laboratory and field data to quantify the immersion freezing ice nucleation activity of mineral
1416 dust particles, *Atmos. Chem. Phys. Discuss.*, 14, 17359–17400, doi:10.5194/acpd-14-17359-
1417 2014, 2014.

1418

1419 Diehl, K., Mitra, S. K., Szakáll, M., Blohn, N. v., Borrmann, S., and Pruppacher, H.R.:
1420 Chapter 2. Wind Tunnels: Aerodynamics, Models, and Experiments. In: *The Mainz Vertical*
1421 *Wind Tunnel Facility: A Review of 25 Years of Laboratory Experiments on Cloud Physics*
1422 *and Chemistry* [Pereira, J. D. (eds.)], Nova Science Publishers, Inc., Hauppauge, NY, USA,
1423 2011.

1424

1425 Diehl, K., Debertshäuser, M., Eppers, O., Schmithüsen, H., Mitra, S.K., and Borrmann, S.:
1426 Particle-area dependence of mineral dust in the immersion mode: investigations with freely
1427 suspended drops in an acoustic levitator. *Atmos. Chem. Phys.*, 14, 12343–12355,
1428 doi:10.5194/acp-14-12343-2014, 2014.

1429

1430 Durant, A.J. and Shaw, R. A.: Evaporation freezing by contact nucleation inside-out,
1431 Geophys. Res. Lett., 32, L20814, doi:10.1029/2005GL024175, 2005.
1432
1433 Dymarska, M., Murray, B. J., Sun, L. M., Eastwood, M. L., Knopf, D. A., and Bertram, A. K.:
1434 Deposition ice nucleation on soot at temperatures relevant for the lower troposphere, J.
1435 Geophys. Res., 111, D04204, doi:10.1029/2005JD006627, 2006.
1436
1437 Ervens, B. and Feingold, G.: Sensitivities of immersion freezing: Reconciling classical
1438 nucleation theory and deterministic expressions, Geophys. Res. Lett., 40, 3320–3324,
1439 doi:10.1002/grl.50580, 2013.
1440
1441 Fletcher, N. H.: Physics of Rain Clouds, Cambridge Univ. Press, New York, NY, USA, 386
1442 pp, 1962.
1443
1444 Fletcher, N. H.: Active sites and ice crystal nucleation, J. Atmos. Sci., 26, 6, 1266–1271,
1445 doi:http://dx.doi.org/10.1175/1520-0469(1969)026<1266:ASAICN>2.0.CO;2, 1969.
1446
1447 Fornea, A.P., Brooks, S. D., Dooley, J. B., and Saha, A. Heterogeneous freezing of ice on
1448 atmospheric aerosols containing ash, soot, and soil, J. Geophys. Res., 114, D13201,
1449 doi:10.1029/2009JD011958, 2009.
1450
1451 Fournier D'albe, E. M.: Some experiments on the condensation of water vapour at
1452 temperatures below 0°C, Q. J. R. Meteorol. Soc., 75, 1–16, doi:10.1002/qj.49707532302,
1453 1949.
1454
1455 Friedman, B., Kulkarni, G., Beránek, J., Zelenyuk, A., Thornton, J. A., and Cziczo, D. J.: Ice
1456 nucleation and droplet formation by bare and coated soot particles, J. Geophys. Res., 116,
1457 D17203, doi:10.1029/2011JD015999, 2011.
1458
1459 Friedrich, F., Studel, A., and Weidler, P. G.: Change of the refractive index of illite particles
1460 by reduction of the Fe content of the octahedral sheet, Clays Clay Miner., 56, 505–510,
1461 doi:10.1346/CCMN.2008.0560503, 2008.
1462
1463 Garimella, S., Huang, Y.-W., Seewald, J. S., and Cziczo, D. J.: Cloud condensation nucleus
1464 activity comparison of dry- and wet-generated mineral dust aerosol: the significance of
1465 soluble material, Atmos. Chem. Phys., 14, 6003–6019, doi:10.5194/acp-14-6003-2014, 2014.
1466
1467 Gregg, S. L. and Sing, K. S. W.: Adsorption, Surface Area and Porosity, Academic Press,
1468 London, UK, 303 pp, 1982.
1469
1470 Grim, R. E.: Clay mineralogy, McGraw-Hill, New York, USA, 384 pp, 1953.
1471 Hader, J. D., Wright, T. P., and Petters, M. D.: Contribution of pollen to atmospheric ice
1472 nuclei concentrations, Atmos. Chem. Phys., 14, 5433–5449, doi:10.5194/acp-14-5433-2014,
1473 2014.
1474
1475 Hartmann, S., Niedermeier, D., Voigtländer, J., Clauss, T., Shaw, R. A., Wex, H., Kiselev, A.,
1476 and Stratmann, F.: Homogeneous and heterogeneous ice nucleation at LACIS: operating
1477 principle and theoretical studies, Atmos. Chem. Phys., 11, 1753–1767, doi:10.5194/acp-11-
1478 1753-2011, 2011.
1479

1480 Herbert, R. J., Murray, B. J., Whale, T. F., Dobbie, S. J., and Atkinson, J. D.: Representing
1481 time-dependent freezing behaviour in immersion mode ice nucleation, *Atmos. Chem. Phys.*,
1482 14, 8501–8520, doi:10.5194/acp-14-8501-2014, 2014.

1483
1484 Hill, T. C. J., Moffett, B. F., DeMott, P. J., Georgakopoulos, D. G., Stump, W. L., Franc, G.
1485 D.: Measurement of Ice Nucleation-Active Bacteria on Plants and in Precipitation by
1486 Quantitative PCR, *Appl. Environ. Microbiol.*, 80, 1256–1267, doi:10.1128/AEM.02967-13,
1487 2014.

1488
1489 Hiranuma, N., Brooks, S. D., Moffet, R., Glen, A., Laskin, A., Gilles, M. K., Liu, P.,
1490 MacDonald, M. A., Strapp, W., and McFarquhar, G. M.: Chemical characterization of
1491 individual particles and residuals of cloud droplets and ice crystals collected on board research
1492 aircraft in the ISDAC 2008 study, *J. Geophys. Res.*, 118, 6564–6579, doi:10.1002/jgrd.50484,
1493 2013.

1494
1495 Hiranuma, N., Paukert, M., Steinke, I., Zhang, K., Kulkarni, G., Hoose, C., Schnaiter, M.,
1496 Saathoff, H., and Möhler, O.: A comprehensive parameterization of heterogeneous ice
1497 nucleation of dust surrogate: laboratory study with hematite particles and its application to
1498 atmospheric models, *Atmos. Chem. Phys.*, 14, 13145–13158, doi:10.5194/acp-14-13145-
1499 2014, 2014a.

1500
1501 Hiranuma, N., Hoffmann, N., Kiselev, A., Dreyer, A., Zhang, K., Kulkarni, G., Koop, T., and
1502 Möhler, O.: Influence of surface morphology on the immersion mode ice nucleation
1503 efficiency of hematite particles, *Atmos. Chem. Phys.*, 14, 2315–2324, doi:10.5194/acp-14-
1504 2315-2014, 2014b.

1505
1506 Hoffmann, N., Kiselev, A., Rzesanke, D., Duft, D., and Leisner, T.: Experimental
1507 quantification of contact freezing in an electrodynamic balance, *Atmos. Meas. Tech.*, 6, 2373–
1508 2382, doi:10.5194/amt-6-2373-2013, 2013.

1509
1510 Hoose, C., Kristjansson, J. E., Chen, J.-P., and Hazra, A.: A classical-theory-based
1511 parameterization of heterogeneous ice nucleation by mineral dust, soot, and biological
1512 particles in a global climate model, *J. Atmos. Sci.*, 67, 2483–2503,
1513 doi:http://dx.doi.org/10.1175/2010JAS3425.1, 2010.

1514
1515 Hoose, C. and Möhler, O.: Heterogeneous ice nucleation on atmospheric aerosols: a review of
1516 results from laboratory experiments, *Atmos. Chem. Phys.*, 12, 9817–9854, doi:10.5194/acp-
1517 12-9817-2012, 2012.

1518
1519 Hussain, K. and Saunders, C. P. R.: Ice nucleus measurement with a continuous flow
1520 chamber. *Q.J.R. Meteorol. Soc.*, 110: 75–84. doi:10.1002/qj.49711046307, 1984.

1521
1522 Iannone, R., Chernoff, D. I., Pringle, A., Martin, S. T., and Bertram, A. K.: The ice nucleation
1523 ability of one of the most abundant types of fungal spores found in the atmosphere, *Atmos.*
1524 *Chem. Phys.*, 11, 1191–1201, doi:10.5194/acp-11-1191-2011, 2011.

1525
1526 Kanji, Z. A. and Abbatt, J. P. D.: Laboratory studies of ice formation via deposition mode
1527 nucleation onto mineral dust and n-hexane soot samples, *J. Geophys. Res.*, 111, D16204,
1528 doi:10.1029/2005JD006766, 2006.

1529

1530 Kanji, Z. A. and Abbatt, J. P. D.: The University of Toronto Continuous Flow Diffusion
1531 Chamber (UT-CFDC): A simple design for ice nucleation studies, *Aerosol Sci. Technol.*, 43,
1532 730–738. doi:10.1080/02786820902889861, 2009.

1533

1534 Kanji, Z. A., Welti, A., Chou, C., Stetzer, O., and Lohmann, U.: Laboratory studies of
1535 immersion and deposition mode ice nucleation of ozone aged mineral dust particles, *Atmos.*
1536 *Chem. Phys.*, 13, 9097–9118, doi:10.5194/acp-13-9097-2013, 2013.

1537

1538 Kashchiev, D.: *Nucleation: Basic Theory with Applications*, Butterworth-Heinemann, Oxford,
1539 UK, 544 pp, 2000.

1540

1541 Khvorostyanov, V. I. and Curry, J. A.: A new theory of heterogeneous nucleation for
1542 application in cloud and climate models, *Geophys. Res. Lett.*, 27, 4081–4084,
1543 doi:10.1029/1999GL011211, 2000.

1544

1545 Kline, D. B. and Brier, G. W.: Some experiments on the measurement of natural ice nuclei,
1546 *Mon. Wea. Rev.*, 89, 263–272, doi:http://dx.doi.org/10.1175/1520-
1547 0493(1961)089<0263:SEOTMO>2.0.CO;2, 1961.

1548

1549 Knopf, D. A. and Alpert, P. A.: A water activity based model of heterogeneous ice nucleation
1550 kinetics for freezing of water and aqueous solution droplets, *Faraday Discuss.*, 165, 513–534,
1551 doi:10.1039/C3FD00035D, 2013.

1552

1553 Koehler, K. A., Kreidenweis, S. M., DeMott, P. J., Petters, M. D., Prenni, A. J., and
1554 Möhler, O.: Laboratory investigations of the impact of mineral dust aerosol on cold cloud
1555 formation, *Atmos. Chem. Phys.*, 10, 11955–11968, doi:10.5194/acp-10-11955-2010, 2010.

1556

1557 Koop, T., Luo, B., Tsias, A., and Peter, T.: Water activity as the determinant for homogeneous
1558 ice nucleation in aqueous solutions, *Nature*, 406, 611–614, doi:10.1038/35020537, 2000.

1559

1560 Kulkarni, G., Fan, J., Comstock, J. M., Liu, X., and Ovchinnikov, M.: Laboratory
1561 measurements and model sensitivity studies of dust deposition ice nucleation, *Atmos. Chem.*
1562 *Phys.*, 12, 7295–7308, doi:10.5194/acp-12-7295-2012, 2012.

1563

1564 Kumar, P., Sokolik, I. N., and Nenes, A.: Cloud condensation nuclei activity and droplet
1565 activation kinetics of wet processed regional dust samples and minerals, *Atmos. Chem. Phys.*,
1566 11, 8661–8676, doi:10.5194/acp-11-8661-2011, 2011.

1567

1568 Levine, J.: *Statistical Explanation of Spontaneous Freezing of Water Droplets*, NACA Tech.
1569 Notes, no. 2234, 1950.

1570

1571 Lüönd, F., Stetzer, O., Welti, A., and Lohmann, U.: Experimental study on the ice nucleation
1572 ability of size-selected kaolinite particles in the immersion mode, *J. Geophys. Res.*, 115,
1573 D14201, doi:10.1029/2009JD012959, 2010.

1574

1575 Marcolli, C., Gedamke, S., Peter, T., and Zobrist, B.: Efficiency of immersion mode ice
1576 nucleation on surrogates of mineral dust, *Atmos. Chem. Phys.*, 7, 5081–5091,
1577 doi:10.5194/acp-7-5081-2007, 2007.

1578

1579 Marcolli, C.: Deposition nucleation viewed as homogeneous or immersion freezing in pores
1580 and cavities, *Atmos. Chem. Phys.*, 14, 2071–2104, doi:10.5194/acp-14-2071-2014, 2014.

1581
1582 Meunier, A.: *Clays*, Springer, 472pp, 2005.
1583
1584 Meunier, A., and Velde.: *Illite: Origins, Evolution and Metamorphism*, Springer, 286pp, 2004.
1585
1586 Möhler, O., Stetzer, O., Schaefers, S., Linke, C., Schnaiter, M., Tiede, R., Saathoff, H.,
1587 Krämer, M., Mangold, A., Budz, P., Zink, P., Schreiner, J., Mauersberger, K., Haag, W.,
1588 Kärcher, B., and Schurath, U.: Experimental investigation of homogeneous freezing of
1589 sulphuric acid particles in the aerosol chamber AIDA, *Atmos. Chem. Phys.*, 3, 211–223,
1590 doi:10.5194/acp-3-211-2003, 2003.
1591
1592 Mullin, J. W.: *Crystallization*, Elsevier Butterworth-Heinemann, Oxford, UK, Forth edn., 600
1593 pp, 2001.
1594
1595 Murray, B. J., Broadley, S. L., Wilson, T. W., Bull, S. J., Wills, R. H., Christenson, H. K., and
1596 Murray, E. J.: Kinetics of the homogeneous freezing of water, *Phys. Chem. Chem. Phys.*, 12,
1597 10380–10387, doi:10.1039/c003297b, 2010.
1598
1599 Murray, B. J., Broadley, S. L., Wilson, T. W., Atkinson, J. D., and Wills, R. H.:
1600 Heterogeneous freezing of water droplets containing kaolinite particles, *Atmos. Chem. Phys.*,
1601 11, 4191–4207, doi:10.5194/acp-11-4191-2011, 2011.
1602
1603 Murray, B. J., O’Sullivan, D., Atkinson, J. D., and Webb, M. E.: Ice nucleation by particles
1604 immersed in supercooled cloud droplets, *Chem. Soc. Rev.*, 41, 6519–6554,
1605 doi:10.1039/c2cs35200a, 2012.
1606
1607 Niedermeier, D., Shaw, R. A., Hartmann, S., Wex, H., Clauss, T., Voigtländer, J., and
1608 Stratmann, F.: Heterogeneous ice nucleation: exploring the transition from stochastic to
1609 singular freezing behavior, *Atmos. Chem. Phys.*, 11, 8767–8775, doi:10.5194/acp-11-8767-
1610 2011, 2011.
1611
1612 Niedermeier, D., Ervens, B., Clauss, T., Voigtländer, J., Wex, H., Hartmann, S., and
1613 Stratmann, F.: A computationally efficient description of heterogeneous freezing: A
1614 simplified version of the soccer ball model, *Geophys. Res. Lett.*, 41, 736–741,
1615 doi:10.1002/2013GL058684, 2014.
1616
1617 Niehaus, J., Bunker, K. W., China, S., Kostinski, A., Mazzoleni, C., Cantrell, W.: A technique
1618 to measure ice nuclei in the contact mode, *J. Atmos. Oceanic Technol.*, 31, 913–922,
1619 doi:http://dx.doi.org/10.1175/JTECH-D-13-00156.1, 2014.
1620
1621 Niemand, M., Möhler, O., Vogel, B., Vogel, H., Hoose, C., Connolly, P., Klein, H.,
1622 Bingemer, H., DeMott, P., and Skrotzki, J.: A particle-surface-area-based parameterization of
1623 immersion freezing on desert dust particles, *J. Atmos. Sci.*, 69, 3077–3092, doi:10.1175/Jas-
1624 D-11-0249.1, 2012.
1625
1626 O’Sullivan, D., Murray, B. J., Malkin, T. L., Whale, T. F., Umo, N. S., Atkinson, J. D., Price,
1627 H. C., Baustian, K. J., Browse, J., and Webb, M. E.: Ice nucleation by fertile soil dusts:
1628 relative importance of mineral and biogenic components, *Atmos. Chem. Phys.*, 14, 1853–
1629 1867, doi:10.5194/acp-14-1853-2014, 2014.
1630

1631 Palmer, H. P., Natural ice-particle nuclei, *Q. J. R. Meteorol. Soc.*, 75, 17–22,
1632 doi:10.1002/qj.49707532303, 1949.
1633
1634 Prenni, A. J., DeMott, P. J., Rogers, D. C., Kreidenweis, S. M., McFarquhar, G. M., Zhang,
1635 G., and Poellot, M. R.: Ice nuclei characteristics from M-PACE and their relation to ice
1636 formation in clouds, *Tellus*, 61B, 436–448, doi:10.1111/j.1600-0889.2009.00415.x, 2009.
1637
1638 Quantachrome Instruments.: autosorb iQ/ASiQwin Operating Manual, Sect. J. Theory and
1639 Discussion, 359–360 pp, 2013.
1640
1641 Riechers, B., Wittbracht, F., Hütten, A., and Koop, T.: The homogeneous ice nucleation rate
1642 of water droplets produced in a microfluidic device and the role of temperature uncertainty,
1643 *Phys. Chem. Chem. Phys.*, 15, 5873–5887, doi:10.1039/c3cp42437e, 2013.
1644
1645 Rogers, D. C.: Development of a continuous flow thermal gradient diffusion chamber for ice
1646 nucleation studies, *Atmos. Res.*, 22, 149–181, doi:10.1016/0169-8095(88)90005-1, 1988.
1647
1648 Rogers, D. C., DeMott, P. J., Kreidenweis, S. M., and Chen, Y.: A continuous-flow diffusion
1649 chamber for airborne measurements of ice nuclei, *J. Atmos. Oceanic Technol.*, 18, 725–741,
1650 doi:http://dx.doi.org/10.1175/1520-0426(2001)018<0725:ACFDCF>2.0.CO;2, 2001.
1651
1652 Rosenfeld, D. and Woodley, W. L.: Deep convective clouds with sustained supercooled liquid
1653 water down to -37.5 °C, *Nature*, 405, 440–442, doi:10.1038/35013030, 2000.
1654
1655 Schill, G. P. and Tolbert, M. A.: Heterogeneous ice nucleation on phase-separated organic-
1656 sulfate particles: effect of liquid vs. glassy coatings, *Atmos. Chem. Phys.*, 13, 4681–4695,
1657 doi:10.5194/acp-13-4681-2013, 2013.
1658
1659 Steinke, I., Möhler, O., Kiselev, A., Niemand, M., Saathoff, H., Schnaiter, M., Skrotzki, J.,
1660 Hoose, C., and Leisner, T.: Ice nucleation properties of fine ash particles from the
1661 Eyjafjallajökull eruption in April 2010, *Atmos. Chem. Phys.*, 11, 12945–12958,
1662 doi:10.5194/acp-11-12945-2011, 2011.
1663
1664 Stetzer, O., Baschek, B., Luond, F., and Lohmann, U.: The Zurich Ice Nucleation Chamber
1665 (ZINC) – A new instrument to investigate atmospheric ice formation, *Aerosol Sci. Technol.*,
1666 42, 64–74, doi:10.1080/02786820701787944, 2008.
1667
1668 Sullivan, R. C., Moore, M. J. K., Petters, M. D., Kreidenweis, S. M., Qafoku, O., Laskin, A.,
1669 Roberts, G. C., and Prather, K. A.: Impact of particle generation method on the apparent
1670 hygroscopicity of insoluble mineral particles, *Aerosol Sci. Tech.*, 44, 830–846, doi:
1671 10.1080/02786826.2010.497514, 2010.
1672
1673 Szakáll, M., Diehl, K., Mitra, S. K., and Borrmann, S.: A wind tunnel study on the shape,
1674 oscillation, and internal circulation of large raindrops with sizes between 2.5 and 7.5 mm, *J.*
1675 *Atmos. Sci.*, 66, 755–765, doi:http://dx.doi.org/10.1175/2008JAS2777.1, 2009.
1676
1677 Tajiri, T., Yamashita, K., Murakami, M., Orikasa, N., Saito, A., Kusunoki, K., and Lilie, L.: A
1678 novel adiabatic-expansion-type cloud simulation chamber. *J. Meteor. Soc. Japan*, 91, 5, 687–
1679 704, doi:http://dx.doi.org/10.2151/jmsj.2013-509, 2013.
1680

1681 Tobo, Y., Prenni, A. J., DeMott, P. J., Huffman, J. A., McCluskey, C. S., Tian, G.,
1682 Pöhlker, C., Pöschl, U., and Kreidenweis, S. M.: Biological aerosol particles as a key
1683 determinant of ice nuclei populations in a forest ecosystem, *J. Geophys. Res. Atmos.*, 118,
1684 10,100–10,110, doi:10.1002/jgrd.50801, 2013.

1685
1686 Tomlinson, E. M. and Fukuta, N.: A new horizontal gradient, continuous flow, ice thermal
1687 diffusion chamber. *J. Atmos. Oceanic Technol.*, 2, 448–467, doi:10.1175/1520-
1688 0426(1985)002<0448:ANHGCF>2.0.CO;2., 1985.

1689
1690 Vali, G.: Nucleation terminology, *J. Aerosol Sci.*, 16, 575–576, doi:10.1016/0021-
1691 8502(85)90009-6, 1985.

1692
1693 Vali, G.: Freezing rate due to heterogeneous nucleation, *J. Atmos. Sci.*, 51, 1843–1856,
1694 doi:http://dx.doi.org/10.1175/1520-0469(1994)051<1843:FRDTHN>2.0.CO;2, 1994.

1695
1696 Vali, G.: Repeatability and randomness in heterogeneous freezing nucleation, *Atmos. Chem.*
1697 *Phys.*, 8, 5017–5031, doi:10.5194/acp-8-5017-2008, 2008.

1698
1699 Vali, G.: Interpretation of freezing nucleation experiments: singular and stochastic; sites and
1700 surfaces, *Atmos. Chem. Phys.*, 14, 5271–5294, doi:10.5194/acp-14-5271-2014, 2014.

1701
1702 Veghte, D. P. and Freedman, M. A.: Facile method for determining the aspect ratios of
1703 mineral dust aerosol by electron microscopy, *Aerosol Sci. Technol.*, 48, 715–724,
1704 doi:10.1080/02786826.2014.920484, 2014.

1705
1706 Wagner, R., Möhler, O., Saathoff, H., Schnaiter, M., and Leisner, T.: New cloud chamber
1707 experiments on the heterogeneous ice nucleation ability of oxalic acid in the immersion mode,
1708 *Atmos. Chem. Phys.*, 11, 2083–2110, doi:10.5194/acp-11-2083-2011, 2011.

1709
1710 Waseda, Y., Matsubara, E., and Shinoda, K.: X-Ray Diffraction Crystallography:
1711 Introduction, Examples and Solved Problems, Springer, 310 pp, 2011.

1712
1713 Wegener, A.: *Thermodynamik der Atmosphäre*. J. A. Barth Verlag, 311 pp, 1911.

1714
1715 Welti, A., Lüönd, F., Stetzer, O., and Lohmann, U.: Influence of particle size on the ice
1716 nucleating ability of mineral dusts, *Atmos. Chem. Phys.*, 9, 6705–6715, doi:10.5194/acp-9-
1717 6705-2009, 2009.

1718
1719 Welti, A., Lüönd, F., Kanji, Z. A., Stetzer, O., and Lohmann, U.: Time dependence of
1720 immersion freezing: an experimental study on size selected kaolinite particles, *Atmos. Chem.*
1721 *Phys.*, 12, 9893–9907, doi:10.5194/acp-12-9893-2012, 2012.

1722
1723 Welti, A., Kanji, Z. A., Lüönd, F., Stetzer, O., and Lohmann, U.: Exploring the mechanisms
1724 of ice nucleation on kaolinite: from deposition nucleation to condensation freezing, *J. Atmos.*
1725 *Sci.*, 71, 16–36, doi:10.1175/JAS-D-12-0252.1, 2014.

1726
1727 Welton, J. E.: *SEM Petrology Atlas*, The American Association of Petroleum Geologists,
1728 Tulsa, OK, USA, 240 pp, 1984.

1729
1730 Wex, H., DeMott, P. J., Tobo, Y., Hartmann, S., Rösch, M., Clauss, T., Tomsche, L.,
1731 Niedermeier, D., and Stratmann, F.: Kaolinite particles as ice nuclei: learning from the use of

- 1732 different kaolinite samples and different coatings, *Atmos. Chem. Phys.*, 14, 5529–5546,
1733 doi:10.5194/acp-14-5529-2014, 2014.
- 1734
- 1735 Wheeler, M. J., Mason, R. H., Steunenberg, K., Wagstaff, M., Chou, C. and Bertram, A. K.:
1736 Immersion freezing of supermicron mineral dust particles: freezing results, testing different
1737 schemes for describing ice nucleation, and ice nucleation active site densities, *J. Phys. Chem.*
1738 *A*, Article ASAP, doi: 10.1021/jp507875q, 2014.
- 1739
- 1740 Wilson, M. J.: Sheet Silicates: Clay Minerals In: *Rock-Forming Minerals*, Volume 3C, [Deer,
1741 W. A., R. A. Howie and J. Zussman (eds.)]. The Geological Society, 736 pp, 2013.
- 1742
- 1743 Wright, T. P. and Petters, M. D.: The role of time in heterogeneous freezing nucleation, *J.*
1744 *Geophys. Res. Atmos.*, 118, 3731–3743, doi:10.1002/jgrd.50365, 2013.
- 1745
- 1746 Wright, T. P., Petters, M. D., Hader, J. D., Morton, T., and Holder, A. L.: Minimal cooling
1747 rate dependence of ice nuclei activity in the immersion mode, *J. Geophys. Res.-Atmos.*, 118,
1748 1–9, doi:10.1002/jgrd.50810, 2013.

Tables and figures of “A comprehensive laboratory study on the immersion freezing behavior of illite NX particles: a comparison of seventeen ice nucleation measurement techniques”

Corresponding Author

Naruki Hiranuma^{a,*}: seong.moon@kit.edu

INUIT project partners (alphabetical order)

Stefanie Augustin-Bauditz^b: augustin@tropos.de
Heinz Bingemer^c: Bingemer@iau.uni-frankfurt.de
Carsten Budke^d: carsten.budke@uni-bielefeld.de
Joachim Curtius^c: curtius@iau.uni-frankfurt.de
Anja Danielczok^c: Danielczok@iau.uni-frankfurt.de
Karoline Diehl^e: kdiehl@uni-mainz.de
Katharina Dreischmeier^d:
katharina.dreischmeier@uni-bielefeld.de
Martin Ebert^f: mebert@geo.tu-darmstadt.de
Fabian Frank^c: frank@iau.uni-frankfurt.de
Nadine Hoffmann^a: nadine.hoffmann@kit.edu
Konrad Kandler^f: kandler@geo.tu-darmstadt.de
Alexei Kiselev^a: alexei.kiselev@kit.edu
Thomas Koop^d: thomas.koop@uni-bielefeld.de
Thomas Leisner^a: thomas.leisner@kit.edu
Ottmar Möhler^a: ottmar.moehler@kit.edu
Björn Nillius^{c,n}: b.nillius@mpic.de
Andreas Peckhaus^a: andreas.peckhaus@kit.edu
Diana Rose^c: rose@iau.uni-frankfurt.de
Stephan Weinbruch^f:
weinbruch@geo.tu-darmstadt.de
Heike Wex^b: wex@tropos.de

Associated partners (alphabetical order)

Yvonne Boose^g: yvonne.boose@env.ethz.ch
Paul J. DeMott^h: pdemott@lamar.colostate.edu
John D. Haderⁱ: jdhader@ncsu.edu
Thomas C. J. Hill^h: Thomas.Hill@ColoState.EDU
Zamin A. Kanji^g: zamin.kanji@env.ethz.ch
Gourihar Kulkarni^l: Gourihar.Kulkarni@pnnl.gov
Ezra J. T. Levin^h: e Levin@atmos.colostate.edu
Christina S. McCluskey^h:
mccluscs@atmos.colostate.edu
Masataka Murakami^k: mamuraka@mri-jma.go.jp
Benjamin J. Murray^l: B.J.Murray@leeds.ac.uk
Dennis Niedermeier^{b,o}: niederm@tropos.de
Markus D. Pettersⁱ: markus_petters@ncsu.edu
Daniel O’Sullivan^l: D.OSullivan@leeds.ac.uk
Atsushi Saito^k: asaito@mri-jma.go.jp
Gregory P. Schill^m: gregory.schill@colorado.edu
Takuya Tajiri^k: ttajiri@mri-jma.go.jp
Margret A. Tolbert^m: tolbert@colorado.edu
André Welti^g: andre.welti@env.ethz.ch
Thomas F. Whale^l: eetfw@leeds.ac.uk
Timothy P. Wright^l: timothy.wright@gmail.com
Katsuya Yamashita^{k,p}: yamashita@bosai.go.jp

-  ^aInstitute for Meteorology and Climate Research – Atmospheric Aerosol Research, Karlsruhe Institute of Technology, Karlsruhe, Germany.
-  ^bLeibniz Institute for Tropospheric Research, Leipzig, Germany.
-  ^cInstitute for Atmospheric Physics, University of Mainz, Mainz, Germany.
-  ^dFaculty of Chemistry, Bielefeld University, Bielefeld, Germany.
-  ^eInstitute for Atmospheric and Environmental Science, Goethe University of Frankfurt, Frankfurt, Germany.
-  ^fInstitute of Applied Geosciences, Technical University Darmstadt, Germany.
-  ^gInstitute for Atmosphere and Climate Science, ETH, Zurich, Switzerland.
-  ^hDepartment of Atmospheric Science, Colorado State University, Fort Collins, CO, USA.
-  ⁱDepartment of Marine Earth and Atmospheric Sciences, North Carolina State University, Raleigh, NC, USA.
-  ^jAtmospheric Science and Global Change Division, Pacific Northwest National Laboratory, Richland, WA, USA.
-  ^kMeteorological Research Institute (MRI), Tsukuba, Japan.
-  ^lInstitute for Climate and Atmospheric Science, School of Earth and Environment, University of Leeds, Leeds, UK.
-  ^mCooperative Institute for Research in Environmental Sciences and Department of Chemistry and Biochemistry, University of Colorado, Boulder, CO, USA.
-  Now at, ⁿMax-Planck-Institut für Chemie, Mainz, Germany.
-  Now at, ^oDepartment of Physics, Michigan Technological University, Houghton, MI, USA.
-  Now at, ^pSnow and Ice Research Center, Nagaoka, Japan.

Citation:

N. Hiranuma, et al. **A comprehensive laboratory study on the immersion freezing behavior of illite NX particles: a comparison of seventeen ice nucleation measurement techniques**, for *Atmospheric Chemistry and Physics* – **Special Issue: Results from the ice nuclei research unit (INUIT)**.

Table 1. Summary of INUIT measurement techniques and instruments. All acronyms are available in the Supplementary Information Sect. S4. Note ‘poly’ and ‘mono’ denote polydisperse and quasi-monodisperse size-selected particle distributions, respectively.

ID	Instrument	Description	Portable ?	Reference	Investigable T range	Ice detected T range for this study
1	BINARY*	Cold stage-supported droplet assay	No	<i>Budke and Koop.</i> , 2014	$-25\text{ }^{\circ}\text{C} < T < \sim 0\text{ }^{\circ}\text{C}$	$-24\text{ }^{\circ}\text{C} < T < -15\text{ }^{\circ}\text{C}$
2	CSU-IS	Immersion mode ice spectrometer	Yes	<i>Hill et al.</i> , 2014	$-30\text{ }^{\circ}\text{C} < T < \sim 0\text{ }^{\circ}\text{C}$	poly: $-25\text{ }^{\circ}\text{C} < T < -11\text{ }^{\circ}\text{C}$ mono: $-26\text{ }^{\circ}\text{C} < T < -20\text{ }^{\circ}\text{C}$
3	Leeds-NIPI	Nucleation by immersed particles instrument	No	<i>O’Sullivan et al.</i> , 2014	$-36\text{ }^{\circ}\text{C} < T < \sim 0\text{ }^{\circ}\text{C}$	$-21\text{ }^{\circ}\text{C} < T < -11\text{ }^{\circ}\text{C}$
4	M-AL*	Acoustic droplet levitator	No	<i>Diehl et al.</i> , 2014	$-30\text{ }^{\circ}\text{C} < T < \sim 0\text{ }^{\circ}\text{C}$	$-25\text{ }^{\circ}\text{C} < T < -15\text{ }^{\circ}\text{C}$
5	M-WT*	Vertical wind tunnel	No	<i>Szakáll et al.</i> , 2009; <i>Diehl et al.</i> , 2011	$-30\text{ }^{\circ}\text{C} < T < \sim 0\text{ }^{\circ}\text{C}$	$-21\text{ }^{\circ}\text{C} < T < -19\text{ }^{\circ}\text{C}$
6	NC State-CS	Cold stage-supported droplet assay	No	<i>Wright and Petters</i> , 2013	$-40\text{ }^{\circ}\text{C} < T < \sim 0\text{ }^{\circ}\text{C}$	$-34\text{ }^{\circ}\text{C} < T < -14\text{ }^{\circ}\text{C}$
7	CU-RMCS	Cold stage-supported droplet assay	No	<i>Schill and Tolbert</i> , 2013	$-40\text{ }^{\circ}\text{C} < T < -20\text{ }^{\circ}\text{C}$	$-32\text{ }^{\circ}\text{C} < T < -23\text{ }^{\circ}\text{C}$
8	AIDA*	CECC	No	<i>Möhler et al.</i> , 2003 <i>Hiranuma et al.</i> , 2014a,b	$-100\text{ }^{\circ}\text{C} < T < -5\text{ }^{\circ}\text{C}$	poly: $-35\text{ }^{\circ}\text{C} < T < -27\text{ }^{\circ}\text{C}$ mono: $-34\text{ }^{\circ}\text{C} < T < -28\text{ }^{\circ}\text{C}$
9	CSU-CFDC	Cylindrical plates CFDC	Yes	<i>Tobo et al.</i> , 2013	$-34\text{ }^{\circ}\text{C} < T < -9\text{ }^{\circ}\text{C}$	$-29\text{ }^{\circ}\text{C} < T < -22\text{ }^{\circ}\text{C}$
10	EDB*	Electrodynamic balance levitator	No	<i>Hoffmann et al.</i> , 2013	$-40\text{ }^{\circ}\text{C} < T < -1\text{ }^{\circ}\text{C}$	^a imm.: $-31\text{ }^{\circ}\text{C} < T < -28\text{ }^{\circ}\text{C}$ ^b contact: $-34\text{ }^{\circ}\text{C} < T < -27\text{ }^{\circ}\text{C}$
11	FINCH*	Continuous flow mixing chamber	Yes	<i>Bundke et al.</i> , 2008	$-60\text{ }^{\circ}\text{C} < T < -2\text{ }^{\circ}\text{C}$	$-27\text{ }^{\circ}\text{C} < T < -22\text{ }^{\circ}\text{C}$
12	FRIDGE*	Substrate-supported diffusion and condensation/immersion cell	Yes	<i>Bingemer et al.</i> , 2012	$-25\text{ }^{\circ}\text{C} < T < -8\text{ }^{\circ}\text{C}$	^c default: $-25\text{ }^{\circ}\text{C} < T < -18\text{ }^{\circ}\text{C}$ ^d imm.: $-25\text{ }^{\circ}\text{C} < T < -18\text{ }^{\circ}\text{C}$
13	LACIS*	Laminar flow tube	No	<i>Hartmann et al.</i> , 2011; <i>Wex et al.</i> , 2014	$-40\text{ }^{\circ}\text{C} < T < -5\text{ }^{\circ}\text{C}$	$-37\text{ }^{\circ}\text{C} < T < -31\text{ }^{\circ}\text{C}$
14	MRI-DCECC	Dynamic CECC	No	<i>Tajiri et al.</i> , 2013	$-100\text{ }^{\circ}\text{C} < T < \sim 0\text{ }^{\circ}\text{C}$	poly: $-26\text{ }^{\circ}\text{C} < T < -21\text{ }^{\circ}\text{C}$ mono: $-29\text{ }^{\circ}\text{C} < T < -21\text{ }^{\circ}\text{C}$
15	PINC	Parallel plates CFDC	Yes	<i>Chou et al.</i> , 2011; <i>Kanji et al.</i> , 2013	$-40\text{ }^{\circ}\text{C} < T < -9\text{ }^{\circ}\text{C}$	$-35\text{ }^{\circ}\text{C} < T < -26\text{ }^{\circ}\text{C}$
16	PNNL-CIC	Parallel plates CFDC	Yes	<i>Friedman et al.</i> , 2011	$-55\text{ }^{\circ}\text{C} < T < -15\text{ }^{\circ}\text{C}$	$-35\text{ }^{\circ}\text{C} < T < -27\text{ }^{\circ}\text{C}$
17	IMCA-ZINC	Parallel plates CFDC	No	<i>Lüönd et al.</i> , 2010 <i>Stetzer et al.</i> , 2008; <i>Welti et al.</i> , 2009	$-65\text{ }^{\circ}\text{C} < T < -5\text{ }^{\circ}\text{C}$	^e imm.: $-36\text{ }^{\circ}\text{C} < T < -31\text{ }^{\circ}\text{C}$ ^f ZINC: $-33\text{ }^{\circ}\text{C} < T < -32\text{ }^{\circ}\text{C}$

*Instruments of INUIT project partners, a. immersion freezing, b. contact freezing, c. default deposition nucleation, d. immersion freezing with suspended particles, e. immersion freezing with IMCA, f. ZINC alone.

Table 2. X-ray diffraction analyses of the bulk composition of illite NX powder.

Mineral	Weight Percentage (wt%)			
	This study	Manufacturer Data	Broadley et al., 2012	Friedrich et al., 2008 [†]
Illite	69	86	74	76
Kaolinite	10	10	7	5
Quartz	3	4	7	<1
Calcite/Carbonate	3	N/A	2	2
Feldspar (Orthoclase/Sanidine)	14	N/A	10	4

[†]*Friedrich et al.* (2008) noted 11 wt% additional impurities, including phlogopite (7.8 wt%), anhydrite (1.4 wt%), plagioclase (1.1 wt%), and apatite (0.7 wt%).

Table 3. List of the Gumbel cumulative distribution fit parameters to the $n_{s,BET}$ and $n_{s,geo}$ for T -binned ensemble dataset fitted in the linear space [All (lin)], ensemble dataset fitted in the log space [All (log)], ensemble maximum values (All_{max}), ensemble minimum values (All_{min}), suspension subset fitted in the linear space [Sus (lin)], suspension subset fitted in the log space [Sus (log)], dry-dispersed particle subset fitted in the linear space [Dry (lin)] and dry-dispersed particle subset fitted in the log space [Dry (log)]. Note that All_{max} and All_{min} are fitted in the linear space. The correlation coefficient, r , for each fit is also shown. T is in °C.

Fitted dataset	Fitted T range	Fit Parameters				
		$[n_{s,BET}(T) = \exp(a \cdot \exp(-\exp(b \cdot (T+c))))+d]$				
		a	b	c	d	r
†All (lin)	-37 °C < T < -11 °C	23.82	0.16	17.49	1.39	0.60
†All (log)	-37 °C < T < -11 °C	22.00	0.16	20.07	3.00	0.80
†All _{max}	-37 °C < T < -11 °C	24.72	0.15	17.27	1.56	0.63
†All _{min}	-37 °C < T < -11 °C	21.86	0.16	22.73	2.70	0.94
Sus (lin)	-34 °C < T < -11 °C	24.38	0.14	19.61	1.89	0.99
Sus (log)	-34 °C < T < -11 °C	24.28	0.14	21.19	2.70	0.99
†Dry (lin)	-37 °C < T < -18 °C	27.35	0.07	16.48	3.19	0.59
†Dry (log)	-37 °C < T < -18 °C	26.22	0.07	16.27	3.31	0.72

Fitted dataset	Fitted T range	Fit Parameters				
		$[n_{s,geo}(T) = \exp(a \cdot \exp(-\exp(b \cdot (T+c))))+d]$				
		a	b	c	d	r
†All (lin)	-37 °C < T < -11 °C	25.75	0.13	17.17	3.34	0.73
†All (log)	-37 °C < T < -11 °C	22.93	0.16	20.31	5.72	0.80
†All _{max}	-37 °C < T < -11 °C	25.72	0.15	16.39	3.52	0.75
†All _{min}	-37 °C < T < -11 °C	22.16	0.16	22.13	5.64	0.98
Sus (lin)	-34 °C < T < -11 °C	22.72	0.16	19.52	5.50	1.00
Sus (log)	-34 °C < T < -11 °C	22.64	0.16	20.93	5.92	0.98
†Dry (lin)	-37 °C < T < -18 °C	29.38	0.05	16.49	7.19	0.64
†Dry (log)	-37 °C < T < -18 °C	27.92	0.05	13.25	6.32	0.83

†To derive the fits that are representative for immersion mode freezing, we excluded EDB (contact) and ZINC data.

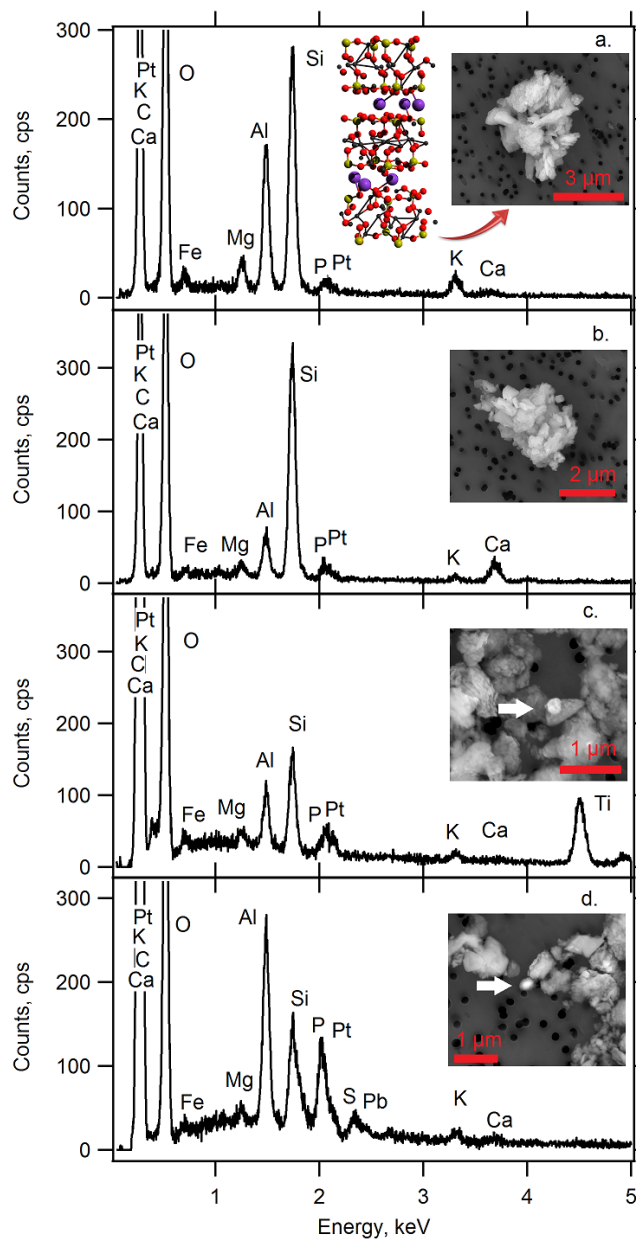


Figure 1. EDX spectra of representative illite NX particles. (a) typical illite, (b) calcite rich mineral, (c) titanium oxide rich mineral, and (d) lead rich mineral. Scanning electron microscopy images of characterized particles are shown in subpanels. A schematic representation of the illite's crystal structure (silicon in yellow, aluminum in black, oxygen in red and potassium in purple) is also shown.

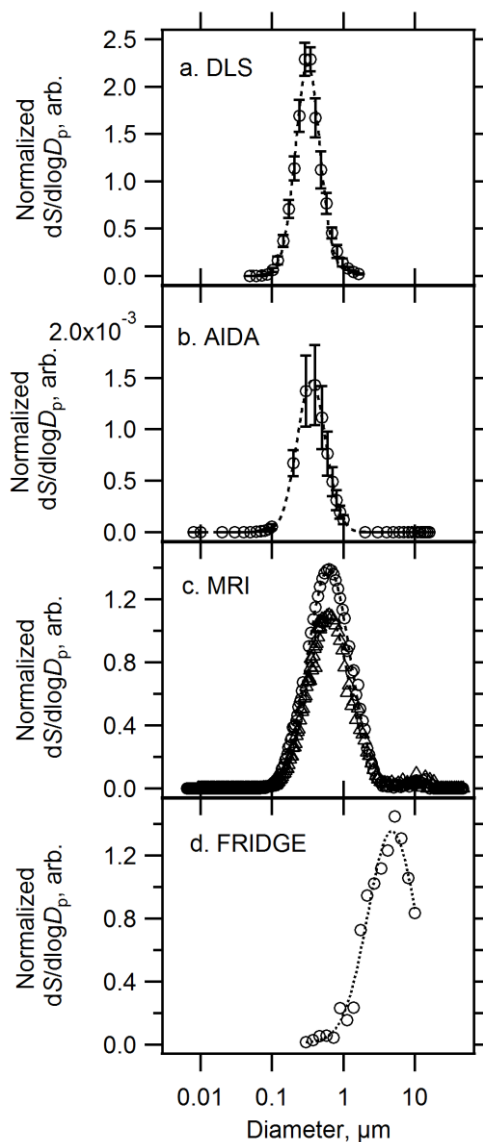


Figure 2. Surface area distributions of (a) suspended and (b-d) dry illite NX particles. Hydrodynamic size-based surface area distributions are measured in suspension using DLS. The average (\pm standard error) of five measurements with different concentrations of suspended illite NX powder (0.05, 0.1, 0.25, 0.5 and 1 mg mL⁻¹) is presented in (a). Volume equivalent diameter-based dry-dispersed particle surface area distributions measured in the AIDA chamber (mean of ten measurements \pm standard error) and MRI-DCECC (two individual measurements) are shown in (b) and (c), respectively. Panel (d) shows optical diameter-based particle surface area distributions measured by a TSI-OPS used for the FRIDGE immersion mode experiments. Dotted lines represent log-normal fits, and corresponding mode diameters are (a) 0.32 μ m, (b) 0.36 μ m, (c) 0.62 μ m and (d) 4.75 μ m. The width-parameters of log-normal fittings are (a) 0.55, (b) 0.65, (c) 0.95 and (d) 1.10.

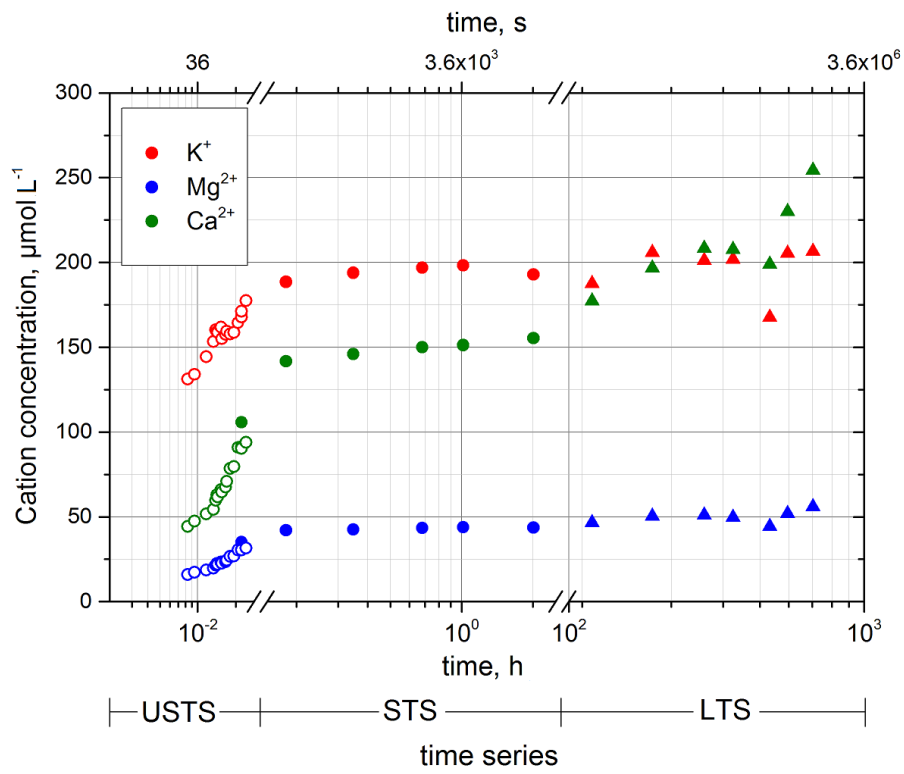


Figure 3. Evolution of the cation concentration in aqueous suspension of 0.1g illite in 10ml deionized water with time. The scaling of the time-axis is different for three different subsections of the time series (USTS, STS and LTS).

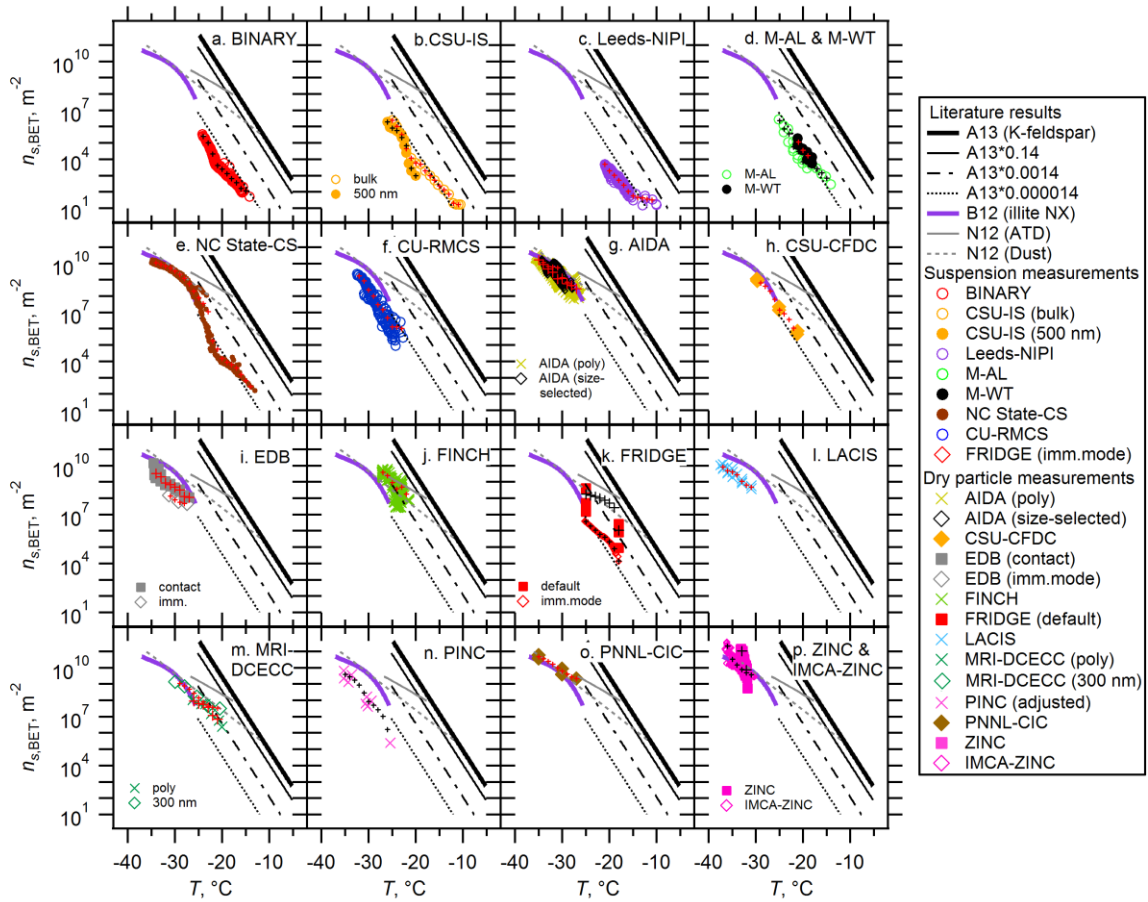


Figure 4. Inter-comparison of seventeen instruments using $n_{s,BET}$. Black or red cross markers are interpolated $n_s(T)$ used for T -binned averaging. Note that M-AL and M-WT results are presented in (d). In (k), FRIDGE results of default (solid square) and imm.mode (open diamond) measurements are presented. Both ZINC (solid square) and IMCA-ZINC (open diamond) data are shown in (p). Reference immersion freezing $n_s(T)$ spectra for illite NX (B12; *Broadley et al.*, 2012), K-feldspar (A13; *Atkinson et al.*, 2013), ATD and desert dusts (Dust) (N12; *Niemand et al.*, 2012) are also shown (See Sect. 3.2).

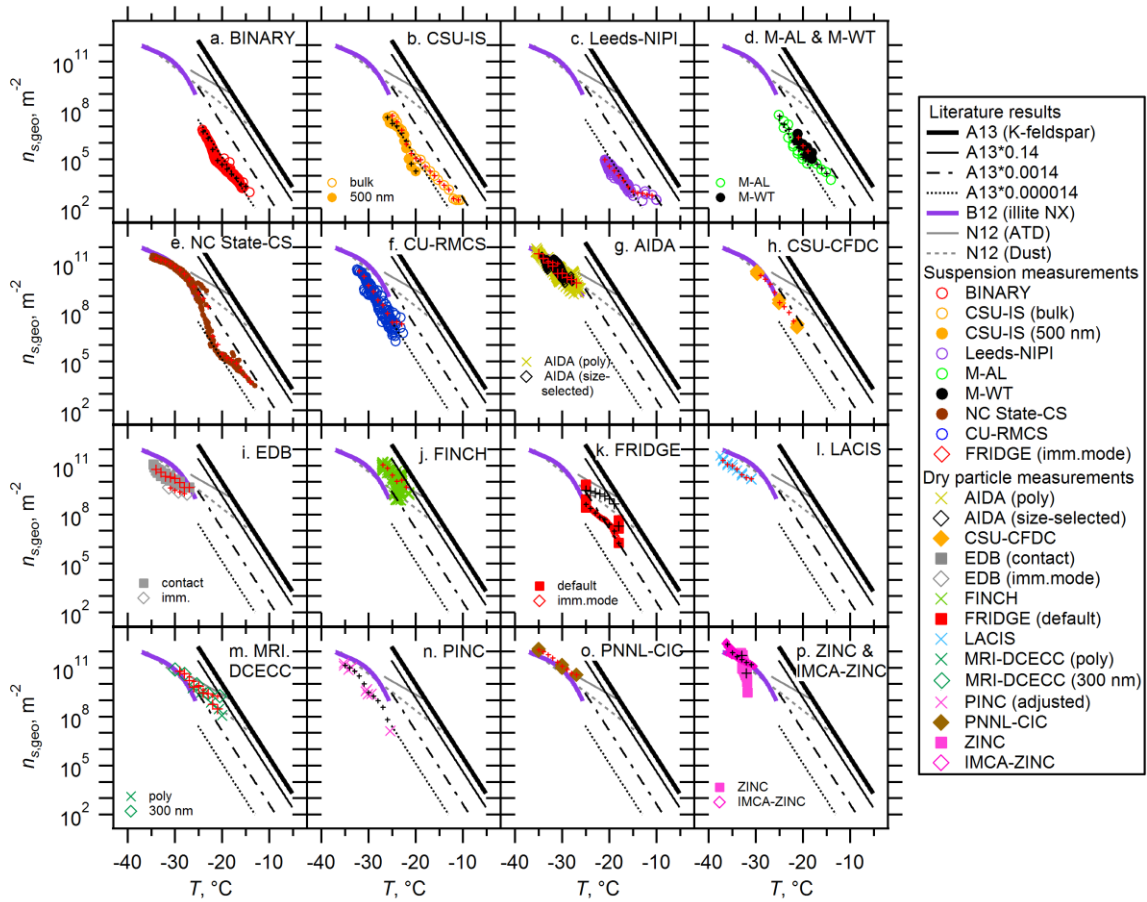


Figure 5. Geometric size-based ice nucleation active surface-site density, $n_{s,geo}$, of seventeen measurement techniques. Black or red cross markers are interpolated $n_s(T)$ used for T -binned averaging. Note that M-AL and M-WT results are presented in (d). In (k), FRIDGE results of default (solid square) and imm.mode (open diamond) are presented. Both ZINC (solid square) and IMCA-ZINC (open diamond) data are shown in (p). Reference immersion freezing $n_s(T)$ spectra are provided as in Fig. 4.

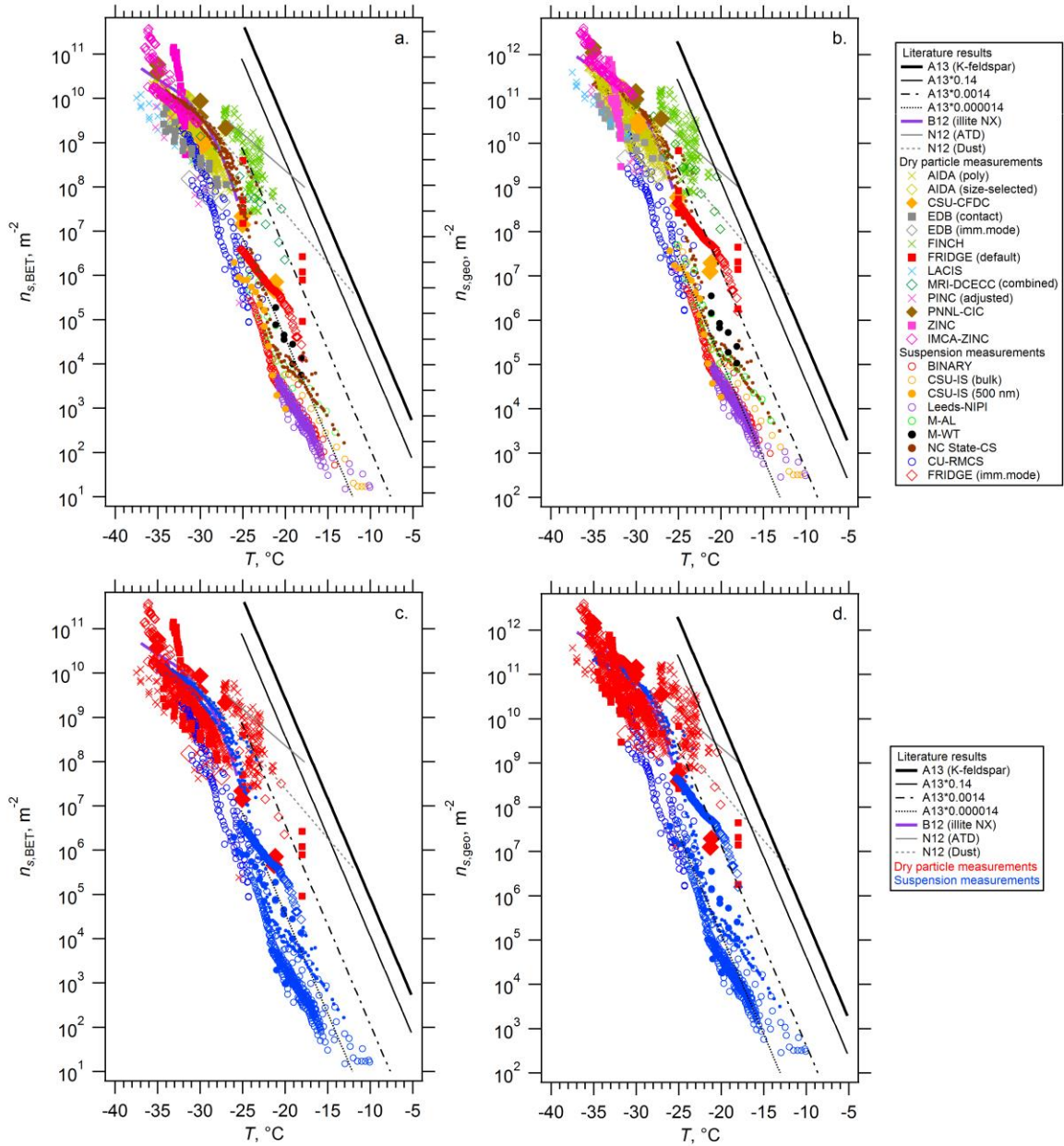


Figure 6. Immersion freezing $n_s(T)$ spectra of illite NX particles from seventeen instruments calculated as a function of the BET (a) and geometric (b) surface areas. Reference immersion freezing $n_s(T)$ spectra are provided as in Figs. 4 and 5. Dry-dispersed particle (red markers) and suspension (blue markers) results for $n_{s,\text{BET}}$ and $n_{s,\text{geo}}$ are shown in (c) and (d), respectively, to highlight the difference between dry particle and suspension subsets.

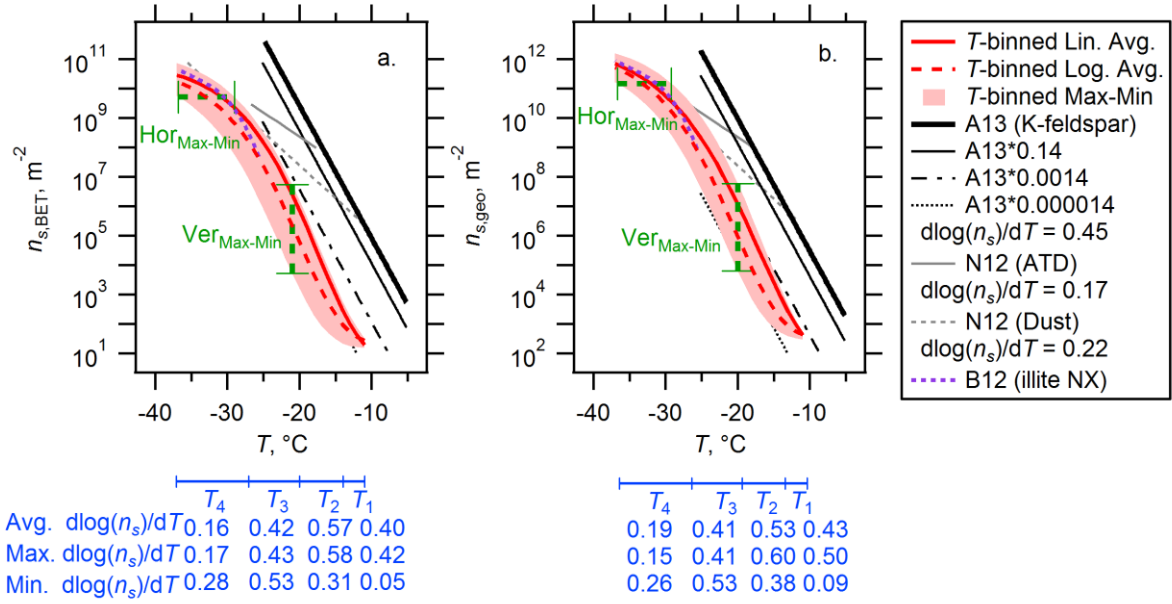


Figure 7. The n_s parameterization, based on the BET (a) and geometric (b) surface areas, as a function of temperature (T). The multiple exponential distribution fit in the linear space (T -binned Lin. Avg.) is expressed as $n_{s,BET}(T) = \exp(23.82 \times \exp(-\exp(0.16 \times (T + 17.49))) + 1.39)$ or $n_{s,geo}(T) = \exp(25.75 \times \exp(-\exp(0.13 \times (T + 17.17))) + 3.34)$. The same fit in the log space (T -binned Log. Avg.) is expressed as $n_{s,BET}(T) = \exp(22.00 \times \exp(-\exp(0.16 \times (T + 20.07))) + 3.00)$ or $n_{s,geo}(T) = \exp(22.93 \times \exp(-\exp(0.16 \times (T + 20.31))) + 5.72)$. Note that n_s and T are in m^{-2} and $^{\circ}C$, respectively. The maximum deviation between maxima and minima in horizontal axis (in T $^{\circ}C$) and vertical axis [in $\log(n_{s,max}/n_{s,min})$] corresponds to $Hor_{Max-Min}$ and $Ver_{Max-Min}$, respectively. All fit parameters are shown in Table 3.

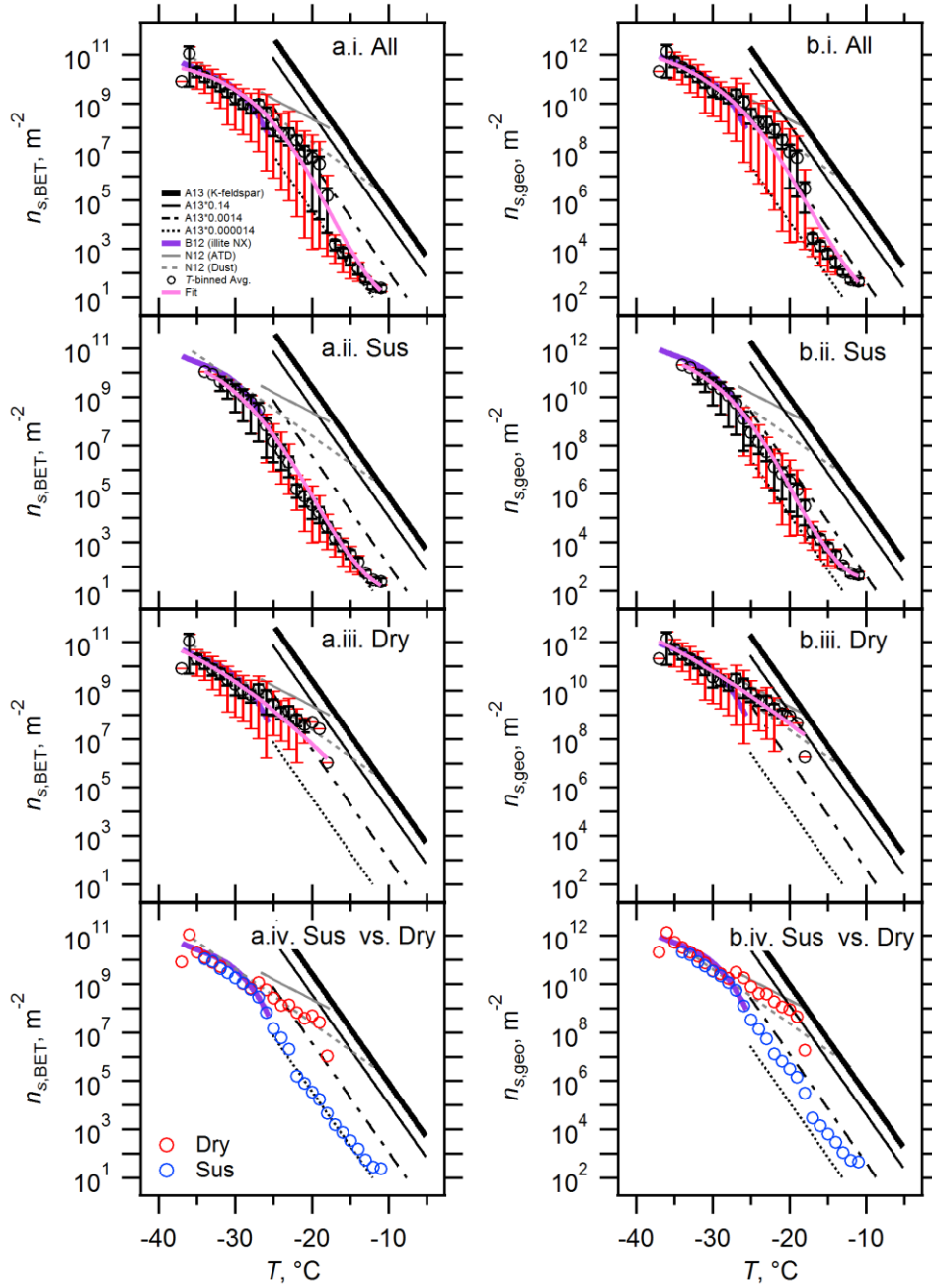


Figure 8. T -binned $n_{s,geo}$ (a) and $n_{s,BET}$ (b). T -binned data (i.e., average in the linear space with 1°C bins for $-37^\circ\text{C} < T < -11^\circ\text{C}$) of $n_s(T)$ spectra are presented for (i) All interpolated dataset (All), (ii) Suspension measurements (Sus), (iii) Dry-dispersed particle measurements (Dry), and (iv) comparison between Sus and Dry. Red sticks represent maxima (positive direction) and minima (negative direction) and black sticks represent \pm standard error. Literature results (B12, A13, and N12) are also shown.

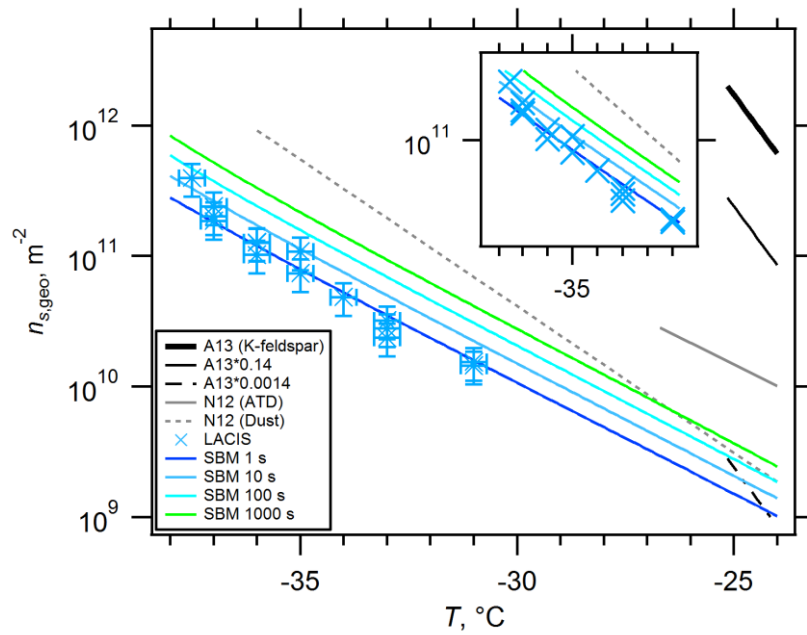


Figure 9. Soccer ball model analysis for time dependency of immersion freezing of illite NX particles. Comparison to LACIS measurements in $n_{s,geo}$ space is also shown. Error bars represent experimental uncertainties ($T \pm 0.3$ °C and $n_s \pm 28\%$). The subpanel shows a magnified section of T (-31 to -38 °C) and $n_{s,geo}$ (1.2×10^{10} to 5.1×10^{11} m⁻²) space without error bars. A shift in the residence time from 1s to 10 s shifts n_s (as well as n_m , not shown) towards higher temperatures by about 1 °C.

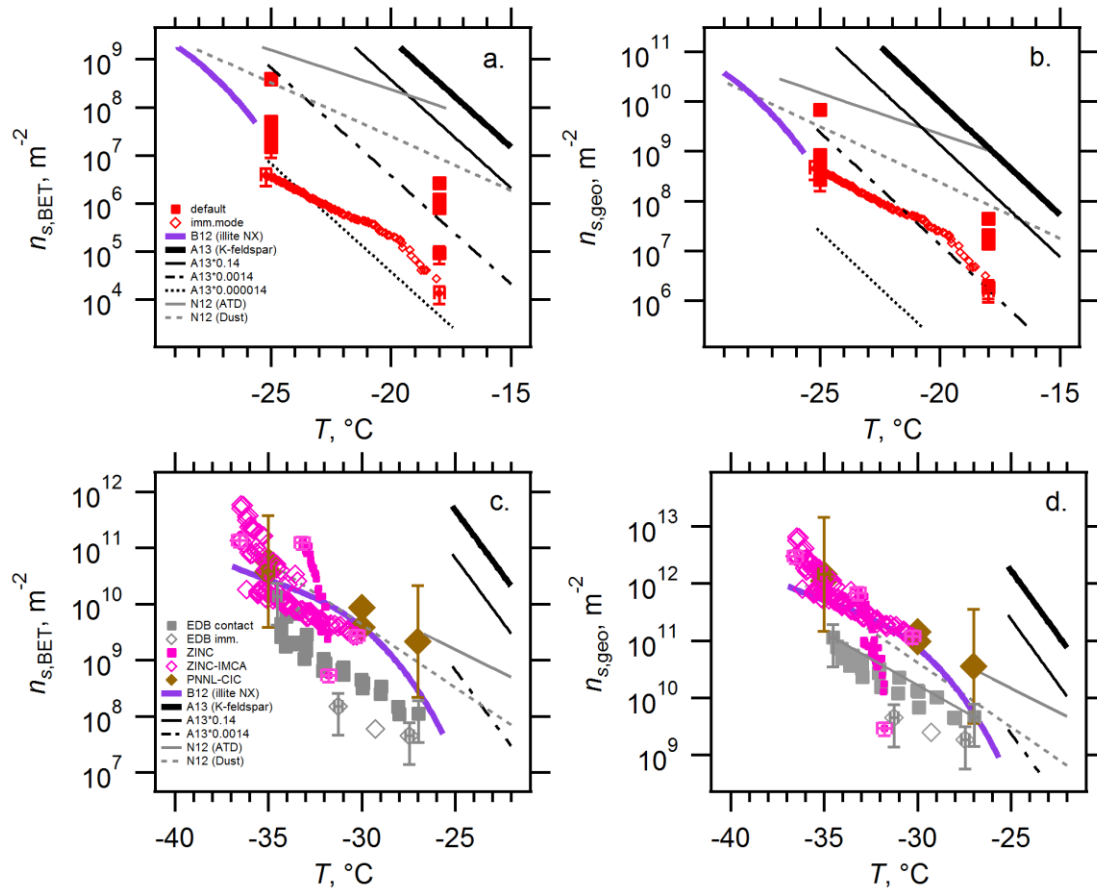


Figure 10. Examination of mode dependency of heterogeneous ice nucleation of illite NX particles. A comparison of FRIDGE (default) and FRIDGE (imm.mode) in $n_{s,BET}$ and $n_{s,geo}$ are shown in (a) and (b), respectively. (c) and (d) show a comparison between EDB (contact), EDB (imm.), ZINC, IMCA-ZINC, and PNNL-CIC data in $n_{s,BET}$ and $n_{s,geo}$, respectively.